

<b>1</b>	<b>Introduction .....</b>	<b>1</b>
1.1	Rydberg Atoms and the Dipole-Dipole Interactions .....	2
1.2	Atomic Units .....	2
1.3	Dissertation Structure .....	3
<b>2</b>	<b>Experimental Setup .....</b>	<b>6</b>
2.1	Magneto-Optical Trap .....	7
2.1.1	Principle of the Magneto-Optical Trap .....	7
2.1.2	Saturated Absorption Spectroscopy .....	11
2.1.3	Ultra High Vacuum Chamber .....	14
2.1.4	Characterization of the MOT .....	14
2.2	Lasers and Amplifiers .....	15
2.2.1	Nd:YAG Lasers .....	15
2.2.2	Diode Lasers .....	17
2.2.3	Mode-Lock Laser .....	17
2.2.4	Chirped Pulse Amplification .....	19
2.2.5	Regenerative Amplifier .....	21
2.2.6	Linear Amplifier .....	22
2.2.7	Dye Laser and Dye Amplifier .....	23
2.3	THz Pulses .....	25
2.4	Detection and Data Collection .....	28
2.4.1	State-Selective Field Ionization .....	28
2.4.2	Synchronization System .....	29
2.4.3	Measurement Operation .....	31
2.5	Maintenance and Daily Operation .....	32

2.5.1	Daily Examination .....	32
2.5.2	Operation of Regenerative Amplifier .....	33
2.5.3	Operation of the MOT .....	34
<b>3</b>	<b>Models in Simulation .....</b>	<b>39</b>
<b>3.1</b>	<b>Rydberg Atoms .....</b>	<b>40</b>
3.1.1	Modern Picture of Rydberg Atoms.....	41
3.1.2	Properties of Rydberg Atoms .....	43
<b>3.2</b>	<b>Two-Body Model.....</b>	<b>44</b>
3.2.1	Introduction to the Two-Body Model.....	44
3.2.2	Nearest Neighbor Distribution .....	45
3.2.3	Förster Resonance Energy Transfer.....	46
<b>3.3</b>	<b>Dipole-Dipole Interaction.....</b>	<b>47</b>
3.3.1	Dipole Moment .....	47
3.3.2	Dipole-Dipole Interaction in the Classical Picture .....	48
3.3.3	Dipole-Dipole Interaction in the Quantum Picture .....	50
3.3.4	Dipole-Dipole Coupled System in an Electric Field .....	53
<b>3.4</b>	<b>Blackbody Radiation Model .....</b>	<b>54</b>
3.4.1	Blackbody Induced Transition .....	55
3.4.2	Radiation Model .....	55
<b>4</b>	<b>Absence of Collective Decay in a Cold Rydberg Gas .....</b>	<b>59</b>
<b>4.1</b>	<b>Introduction.....</b>	<b>60</b>
<b>4.2</b>	<b>Experimental Procedure and Results .....</b>	<b>63</b>
<b>4.3</b>	<b>Analysis and Discussion.....</b>	<b>68</b>
<b>4.4</b>	<b>Conclusion .....</b>	<b>77</b>

<b>5</b>	<b>Rydberg Wavepackets Evolution in A Frozen Gas of DD Coupled Atoms .....</b>	<b>83</b>
5.1	Introduction.....	84
5.2	Experimental Procedure.....	86
5.3	Experimental Results .....	88
5.4	Discussion .....	91
5.5	Conclusion .....	95

Figure 2.1: Simplified one dimensional model for MOT [2].....	8
Figure 2.2: Schematic for MOT design. It's a combination of anti-Helmholtz coils and six counter-propagating laser beams.....	9
Figure 2.3: Hyperfine energy structure of $^{85}\text{Rb}$ . Trap laser drives the transition, $5s_{1/2} F = 3$ to $5p_{3/2} F = 4$ , and the repump laser drives the transition, $5s_{1/2} F = 2$ to $5p_{3/2} F = 3$ . ....	11
Figure 2.4: The saturated absorption spectra for the Rb $5s_{1/2}$ to $5p_{1/2}$ hyperfine transitions and their crossover peaks [3]. Small dark arrows are pointing to the real resonances. Blue dotted arrow, pointing to the side of the crossover peak, indicates where the trap laser is actually locked at. Red dotted arrow indicates the position where the repump laser is locked at. ....	13
Figure 2.5: Schematic of Nd:YAG lasing [6]. It is a typical four-level lasing scheme. ....	16
Figure 2.6: Layout of Continuum Surelite Nd:YAG laser. It can output beams of 4 different frequencies [5].....	16
Figure 2.7: Basic layout of the mode-lock laser [12]. The green line is the pump light from Millennia Vs laser and the red line is the mode-locked beam in the cavity which is centered at 780-800 nm. The prism pair is used to compensate for group velocity dispersion (GVD). By tapping the 2 <sup>nd</sup> prism, we can produce a temporary unstable beam. Stronger intensity part in this beam will be enhanced, producing the periodic pulsed output. ....	18
Figure 2.8: Schematic of chirped pulse amplification system. Seed light is first temporally stretched using the stretcher. Then the stretched pulse gets amplified. Finally the pulse	

is again compressed to something close to its original duration, but with much greater (106-107 times) energy. ....	20
Figure 2.9: Schematic of regenerative amplifier. The switch-in pockels cell controls when a seed pulse is trapped in the resonator and the switch-out pockels cell controls when the pulse is ejected from the cavity. ....	22
Figure 2.10: Schematic of linear amplifier. The beam passes the Nd:YAG pumped gain medium three times and gets amplified.....	23
Figure 2.11: Schematic for a Hansch dye laser and the 2 <sup>nd</sup> harmonic generation. The angle of the tuning grating determines the output frequency. ....	24
Figure 2.12: Schematic for double cell dye amplifier used in the lab. ....	25
Figure 2.13: A typical THz pulse generated in the lab [8]. The duration is about 5 ps and the peak frequency is 0.2-0.4 THz. This pulse is generated using tilted-pulse-front-pumping optical rectification and the temporal profile of the pulse is characterized using the electro-optic sampling method. The frequency spectrum is then derived from the time-domain profile.....	26
Figure 2.14: Schematic of TPFP setup [8]......	27
Figure 2.15: Schematic of the tipping of electron potential. Solid line is the $1/r$ potential when there is no external field applied to the atom. Dashed line shows the tip of potential when a field is applied to the atom. When such a field is strong enough, electrons are able to escape from the trap. ....	29
Figure 2.16: Schematic of the synchronization system. White circles are inputs and dark circles are outputs.....	30

- Figure 2.17: A typical ionization signal shown on an oscilloscope. The central peak representing the population of state  $32s + 32p$ . The measurement program uses a user defined gate and integrates the area under the peak within the gate. ....31
- Figure 2.18: Front view of the chamber where the MOT is positioned in. A, B, and C represent three trap beams. ....36
- Figure 3.1: Classical view of Rydberg orbits of (a) H and (b) Na. In H the electron orbits around the proton. In Na it orbits around the +11 nuclear charge and ten inner shell electrons. In high  $L$  states Na behaves nearly identically to H, but in low  $L$  states the Na electron penetrates and polarizes the inner shell electrons of the Na + core [5]. 41
- Figure 3.2: Schematic of atom pairs in a MOT. For each atom in the MOT, we only consider the effect of its nearest neighbor. One atom and its nearest neighbor is considered to be “a pair of atoms” .....45
- Figure 3.3: Schematic for typical FRET. Black cycles represent the initial pair states and gray cycles the final pair states. (a) is  $pp \rightarrow ss'$ , (b)  $ps \rightarrow sp$  and (c)  $ps' \rightarrow s'p$  [13]. .....47
- Figure 3.4: Schematic of the interaction between two classical dipoles.....50
- Figure 3.5: Schematic for a DD system in an electric field. ....53
- Figure 3.6: Decay model for atoms starting from state  $40s$  as an example. The red dash lines between two states indicate blackbody stimulated transitions between these two states. The blue dash curves represent the spontaneous decay. ....56
- Figure 4.1: (a), (c) Probabilities for finding atoms in  $26s + 25p$  (green, fastest decay),  $32s$  (red, intermediate decay), and  $40s$  (blue, slowest decay) as a function of detection time  $\tau$  for Rydberg densities of  $\rho \sim 3 \times 10^9 \text{ cm}^{-3}$  (a) and  $\rho \sim 1.5 \times 10^8 \text{ cm}^{-3}$  (c). Note that the sum of the  $26s$  and  $25p$  populations is shown since their corresponding features could

not be adequately separated in the field-ionization signal. Vertical bars show the experimental data with uncertainties, and the solid curves are calculated as described in the text. Measurements and calculations for the  $40s$  decay extend to  $500\ \mu s$  where the remaining population is negligible. (b), (d) Probabilities for finding atoms in  $26p$  (green, fastest rise and decay),  $32p$  (red, intermediate rise and decay), and  $40p$  (blue, slowest rise and decay) levels as a function of detection time  $\tau$ . The states are populated by blackbody redistribution from the initial  $26s$ ,  $32s$ , and  $40s$  levels, respectively. The data were measured simultaneously with those shown in (a) and (c). Vertical bars show the experimental data with uncertainties, and the solid curves are calculated as described in the text. The measured  $p$ -state probabilities are normalized to the calculations as described in the text. The calculations have no free parameters and consider only the effects of spontaneous emission and blackbody radiation on isolated atoms. ....66

Figure 4.2: Probabilities for finding atoms in  $26p$  (green, fastest decay),  $32p$  (red, intermediate decay), and  $40p$  (blue, slowest decay) as functions of detection time  $\tau$  for Rydberg densities of  $\rho \sim 3 \times 10^9\ \text{cm}^{-3}$  (a) and  $\rho \sim 1.5 \times 10^9\ \text{cm}^{-3}$  (b). Vertical bars show the experimental data with uncertainties, and the solid curves are calculated as described in the text. Measurements and calculations for the  $40p$  decay extend to  $500\ \mu s$  where the remaining population is negligible. The calculations have no free parameters and consider only the effects of spontaneous emission and blackbody radiation on isolated atoms.....68

Figure 4.3: Measured  $32p_{3/2}\ |m_j| = 1/2$  (bold line) and  $|m_j| = 3/2$  (thin line) excitation probabilities as a function of Rydberg laser frequency in zero applied field. The two data curves are obtained simultaneously in the same laser frequency scan. The small feature on the left (right) of the main  $|m_j| = 1/2$  ( $3/2$ ) peak is the result of imperfect discrimination of the  $|m_j| = 1/2$  and  $3/2$  components via SSFI. The additional peak on

the right of the main feature in each trace is due to the trap-laser dressing of the $5p_{3/2}$ and $5s$ levels. Its frequency shift from the main peak reflects the Autler-Townes splitting of the $5p_{3/2}$ initial state. ....	74
Figure 4.4: Difference (i.e., splitting) in the transition energies for exciting $3p_{3/2}  m_j  = 1/2, 3/2$ from $5p_{3/2}$ as a function of applied electric field. Filled circles are measurements and the solid curve is the result of a numerical Stark map calculation assuming orthogonal “offset” and “residual” electric field components due to the MCP of 2.8 and 1.5 V/cm, respectively. The inset shows a magnified view of the portion of the main figure within the dashed window. ....	75
Figure 5.1: Measured population in the combined $3s+3p$ states as a function of the delay $\Delta t$ between two THz pulses. The left panels show data collected at low Rydberg density, $\rho \sim 3 \times 10^8 \text{ cm}^{-3}$ , for (a) short ( $\Delta t \simeq 0$ ) and (b) long ( $\Delta t \simeq 15 \text{ ns}$ ) delays, respectively. The right panels show data collected at high Rydberg density, $\rho \sim 2 \times 10^9 \text{ cm}^{-3}$ , for c) short ( $\Delta t \simeq 0$ ) and d) long ( $\Delta t \simeq 15 \text{ ns}$ ) delays, respectively. The decrease in oscillation amplitude at high density and long delays is apparent. ....	89
Figure 5.2: Fast Fourier transform (FFT) of the delay-dependent populations shown in Figure 5.1. ....	90
Figure 5.3: Measured (filled circles) and simulated (solid curve) decay ratio, $\eta$ , as a function of Rydberg density. ....	91
Figure 5.4: Schematic energy level diagram for the eigenstates of a pair of two level atoms. The diagrams on the left and right sides of the figure depict the situation at large and small interatomic spacing, $R$ , respectively. ....	93



# 1 Introduction

Rydberg atoms are coupled by long-range dipole-dipole interactions [1]. They attract a lot of attention for their important role in studying fundamental problems as well as potential applications in quantum control in few- and many-body systems, quantum information processing, quantum calculation, etc. [2-10]. The research discussed in this dissertation is focusing on the influence of the DD interactions on the electron dynamics of cold Rydberg atoms. Three projects are presented in this dissertation, including both introduction of experimental setup and simulation results, respectively. Common experimental setups and background knowledge are also provided.

## 1.1 Rydberg Atoms and the Dipole-Dipole Interactions

Rydberg atoms are atoms in which an electron is excited to a state with a high principal quantum number. Usually this number is larger than 10. They are good systems for studying atom dynamics. The details about Rydberg atoms and their properties can be found in references such as [1], and are described in Chapter 3.

Dipole-Dipole interactions can influence neighboring Rydberg atoms. Classically the interaction is the result of the electric forces between electrons and the positively charged ion cores to which they are bound. When coupled by dipole-dipole interactions, Rydberg atoms should not be considered as individuals but rather a system. Details of dipole-dipole interactions, both from classical view and quantum physics prospective, can be found in Chapter 3.

## 1.2 Atomic Units

Atomic units (au or a.u.) are commonly used in atomic physics research. For convenience, we define:

$$\hbar = m_e = e = 4\pi\epsilon_0 = 1 \quad (1.1)$$

where  $\hbar$  is Planck's constant divided by  $2\pi$ ,  $m_e$  is the mass of the electron,  $-e$  is the charge.

We obtain the conversion factors between a.u. and SI units as shown in Table 1.1.

Quantity	Value in atomic units	Value in SI units
Length	1	$5.2917721092(17) \times 10^{-11}$ m
Energy	1	$4.35974417(75) \times 10^{-18}$ J
Time	1	$2.418884326505(16) \times 10^{-17}$ s
Velocity	1	$2.1876912633(73) \times 10^6$ m·s <sup>-1</sup>
Force	1	$8.2387225(14) \times 10^{-8}$ N
Temperature	1	$3.1577464(55) \times 10^5$ K
Pressure	1	$2.9421912(19) \times 10^{13}$ Pa

Electric field	1	$5.14220652(11) \times 10^{11} \text{ V} \cdot \text{m}^{-1}$
Electric potential	1	$2.721138505(60) \times 10^1 \text{ V}$
Electric dipole moment	1	$8.47835326(19) \times 10^{-30} \text{ C} \cdot \text{m}$
Magnetic field	1	$2.35 \times 10^5 \text{ T}$

Table 1.1: Atomic units to SI units conversion factors.

## 1.3 Dissertation Structure

Subsequent chapters describe the experimental approach, numerical simulations and several independent projects. Each project contains both experimental description and simulation description. Additional details and common aspects of all experiments are in chapters 2 and 3.

Chapter 2 provides the information about experimental setups. It introduces the apparatus commonly used in the experiments, as well as the daily operation. More details about some instruments could be found in their respective manuals and the dissertations from previous students who worked in this lab.

Chapter 3 talks about physics concepts commonly involved in the experiments, and their mathematical expression in simulations. It is not practical to put every simulation code line used in this dissertation, but by following the models described in Chapter 3, one could reconstruct the simulations in a fairly straightforward way.

Chapter 4 describes a search for the collective decay in cold Rydberg gases. We found no evidence for superradiance, despite the results reported by other groups. Our analysis suggests that, due to dipole-dipole dephasing, our null result is the expected one.

Chapter 5 describes an exploration of Rydberg wavepacket evolution in dipole-dipole coupled atoms. Our results show, through experiment and simulation, that in dipole-dipole

coupled atoms, the wavepackets are not evolving independently, and variations in the coupling strength between pairs of atoms lead to macroscopic dephasing of the electronic wavepacket motion.

Chapter 6 describes a study of coherence transfer between wavepackets on different atoms via resonant dipole-dipole interactions. We observe evidence for the development of wavepacket motion in one set of atoms driven by wavepacket evolution in neighboring atoms. We confirm the coherence transfer by measuring the relative phase between the initial and induced wavepacket oscillations, suggesting the creation of entangled atom pair states with a dynamically evolving Rydberg wavepacket on one, and only one, atom in each pair. Simulations support our interpretation.

Chapter 7 summarizes the work done in this dissertation and briefly discusses the work in the future.

# Bibliography

- [1] Thomas F. Gallagher. Rydberg Atoms. Cambridge University Press (1994).
- [2] M. D. Lukin, M. Fleischhauer, R. Cote, L. M. Duan, D. Jaksch, J. I. Cirac, and P. Zoller, Phys. Rev. Lett. 87, 037901 (2001).
- [3] D. Tong, S. M. Farooqi, J. Stanojevic, S. Krishnan, Y. P. Zhang, R. Cote, E. E. Eyler, and P. L. Gould, Phys. Rev. Lett. 93, 063001 (2004).
- [4] F. Robicheaux and J. V. Hernandez, Phys. Rev. A 72, 063403 (2005).
- [5] T. Cubel Liebisch, A. Reinhard, P. R. Berman, and G. Raithel, Phys. Rev. Lett. 95, 253002 (2005).
- [6] T. Vogt, M. Viteau, J. Zhao, A. Chotia, D. Comparat, and P. Pillet, Phys. Rev. Lett. 97, 083003 (2006).
- [7] E. Urban, T. A. Johnson, T. Henage, L. Isenhower, D. D. Yavuz, T. G. Walker, and M. Saffman, Nat. Phys. 5, 110 (2009).
- [8] Alpha Gaëtan, Yevhen Miroshnychenko, Tatjana Wilk, Amodsen Chotia, Matthieu Viteau, Daniel Comparat, Pierre Pillet, Antoine Browaeys, and Philippe Grangier, Nat. Phys. 5, 115 (2009).
- [9] T. Wilk, A. Gaetan, C. Evellin, J. Wolters, Y. Miroshnychenko, P. Grangier, and A. Browaeys, Phys. Rev. Lett. 104, 010502 (2010).
- [10] D. Jaksch, J.I. Cirac, P. Zoller, S.L. Rolston, R. Cote, and M.D. Lukin, Phys. Rev. Lett. 85, 2208 (2000).
- [11] A. Dalgarno, Rydberg States of Atoms and Molecules, eds. R. F. Stebbings and F.B. Dunning, Cambridge University Press (1983).
- [12] H. A. Bethe and E.A. Salpeter, Quantum Mechanics of One and Two Electron Atoms, Academic Press (1957).

## 2 Experimental Setup

This chapter contains the general experimental setup for the research discussed in this dissertation. It introduces the apparatus and procedure for state excitation, laser cooling, pulse amplification, THz pulse generation, data collection, etc. It also provides procedures for maintenance and daily operation. All experiments are performed on Newport RS 3000 optical tables to reduce mechanical vibrations, in a temperature controlled room to reduce external thermal fluctuations. Other than specifically noted, the repetition rate of all experiments is 15 Hz. Before beginning experiments in the lab, participants must have taken the laboratory safety training.

## 2.1 Magneto-Optical Trap

Since its invention in 1987 [1], Magneto-Optical Trap (MOT) has become a very important and popular technology in the area of atomic research and has been widely used to generate cold neutral atoms. This technology is a combination of magnetic field gradient and counter-propagating laser beams. The magnetic field gradient generates position dependent energy levels of atoms. Atoms not in the trap center preferentially absorb laser light that tends to push them back to the center.

Due to its ease of operation and low cost, the MOT has been used to trap cold atoms in all the experiments described in this dissertation. We use  $^{85}\text{Rb}$  as the atom source in all experiments. A MOT system contains high vacuum chambers, pump and repump lasers, pressure gauges, atomic beams generation and etc. A very complete and detailed description about this system appears in Mary Kutturf's thesis [4], so only a brief version will be provided here.

### 2.1.1 Principle of the Magneto-Optical Trap

A simplified two-state system can help to understand the trapping process. As shown in Figure 2.1, suppose an atom has a spin  $S = 0$  ground state and spin  $S = 1$  excited states. Assume a weak inhomogeneous magnetic field that varies linearly with  $z$  such that  $B_z(z) = Mz$  where  $M$  is a constant. Due to the Zeeman effect  $\Delta E = \mu m_s B = \mu m_s Mz$ , so the field splits the degeneracy of the excited states, creating position-dependent energies for the atoms. Now assume a beam of  $\sigma_-$  circularly polarized light propagates in the  $-\hat{z}$  direction and another beam with  $\sigma_+$  polarization propagates in the opposite direction. Both beams are red detuned from (i.e. on the low frequency side of) the zero-field resonance.

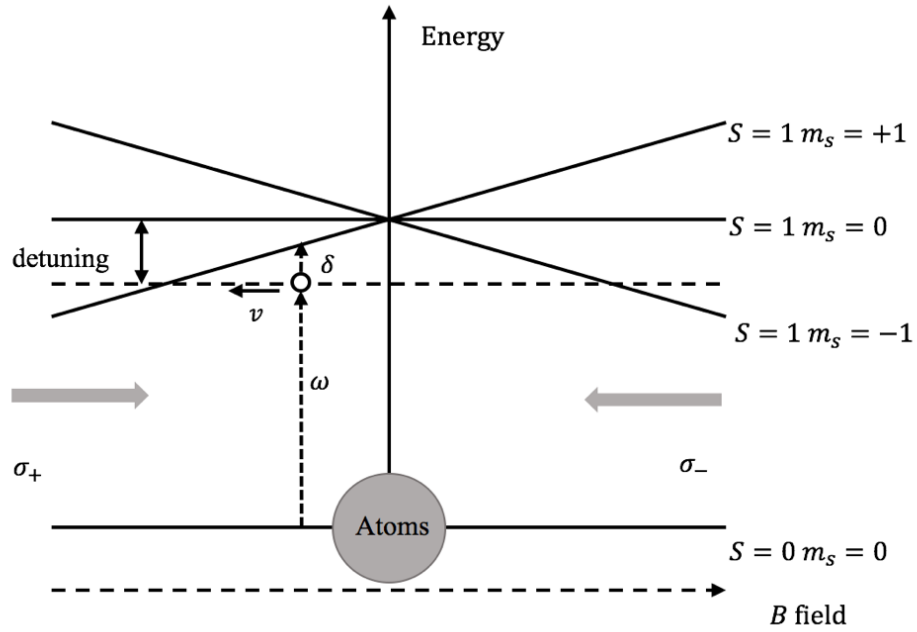


Figure 2.1: Simplified one dimensional model for MOT [2].

Initially, ground state atoms are located in random positions and moving in both directions with random velocities. Suppose an atom passes the center where  $z = 0$ , with a velocity  $-v$  and reaches a  $-z$  position. It encounters the slightly red detuning  $\sigma_+$  beam. Due to Doppler shift, the atom sees photons with a frequency  $\omega + \delta$ , where  $\omega$  is the frequency of the  $\sigma_+$  beam and  $\delta$  is the Doppler shift. When  $\omega + \delta$  is close to the energy gap between the ground state and the excited  $m_s = -1$  state, the atom absorbs a  $\sigma_+$  photon. It later emits a photon through spontaneous decay, but the direction of the emitted photon is random. So the overall effect is that the photon gives the atom a push in  $+z$  direction and this atom has been “slowed down” a little. This process repeats when the atom continues to move in the  $-z$  direction and creates a damped force on the atom. More than that, for a ground atom with position  $z < 0$ , because the energy gap between ground state and the excited  $m_s = -1$  state is smaller than the gap between the ground state and the  $m_s = +1$



state, it is more likely to absorb photons from  $\sigma_+$  beam and get “pushed” towards  $z = 0$ . Similar rules apply to the atoms with position  $z > 0$ . So the motion of an atom in the MOT is similar to a damped harmonic oscillator (for most cases, it is an overdamped harmonic oscillator). The atom is cooled and trapped by the MOT.

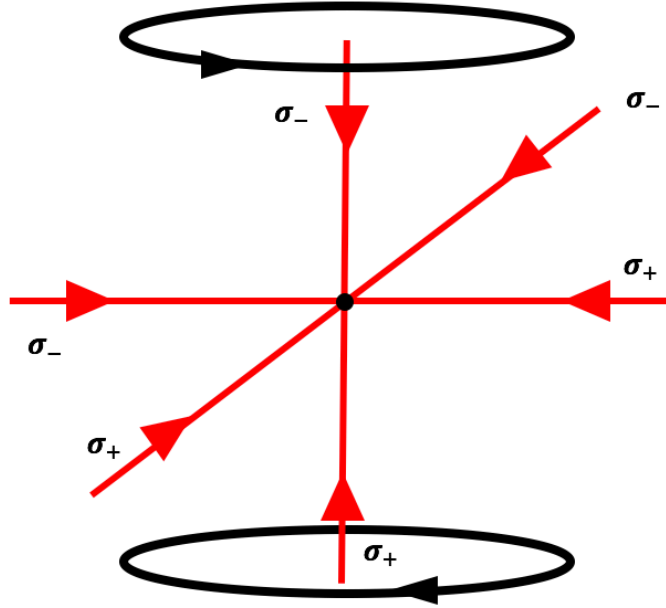


Figure 2.2: Schematic for MOT design. It’s a combination of anti-Helmholtz coils and six counter-propagating laser beams.

As shown in Figure 2.2, a three dimensional Magneto-Optical Trap is an extension of the one dimensional model. The gradient magnetic field in a three dimensional MOT is provided by anti-Helmholtz coils. Other than the main pair of anti-Helmholtz coils shown in this schematic, there are three additional shim coil pairs which enable cancelation of Earth’s magnetic field and fine tuning of the magnetic field inside the MOT. The six laser beams are derived from the same laser. We use three beam splitters to split the primary beam into three equal paths. These three beams are then reflected by mirrors to generate six counter-propagating beams in total. Before retro-reflection, the beam polarizations are

rotated by waveplates placed in front of the mirrors to establish the proper  $\sigma_+$ ,  $\sigma_-$  orientations on each axis.

The above discussion gives an idea about trapping two-level atoms. When dealing with  $^{85}\text{Rb}$ , there are more states involved, although the basic principal is the same as that described above. As shown in Figure 2.3, there are complicated hyperfine levels involved in the trapping of real atoms in a MOT. For  $^{85}\text{Rb}$ ,  $5s_{1/2}$  ground state is split into two hyperfine levels  $F = 2$  and  $F = 3$ . The excited  $5p_{3/2}$  state has been split into four hyperfine levels  $F = 1, 2, 3, 4$ . Ideally, the trap operates on the transfer between two of these levels, from  $5s_{1/2} F = 3$  to  $5p_{3/2} F = 4$ . But because of the small imperfections in the trap laser polarization and the small energy difference between the  $5p_{3/2} F = 3$  and  $5p_{3/2} F = 4$  state, the trap laser transfers a portion of atoms to  $5p_{3/2} F = 3$ . Atoms in  $5p_{3/2} F = 3$  will quickly decay back to  $5s_{1/2} F = 2$  and escape from the MOT. To avoid such a loss, a weaken “repump” laser is introduced into the system. The repump laser transfers the atoms in  $5s_{1/2} F = 2$  back to  $5p_{3/2} F = 3$ . These atoms can later decay back to  $5s_{1/2} F = 3$ , where they continue to cycle via the trap laser.

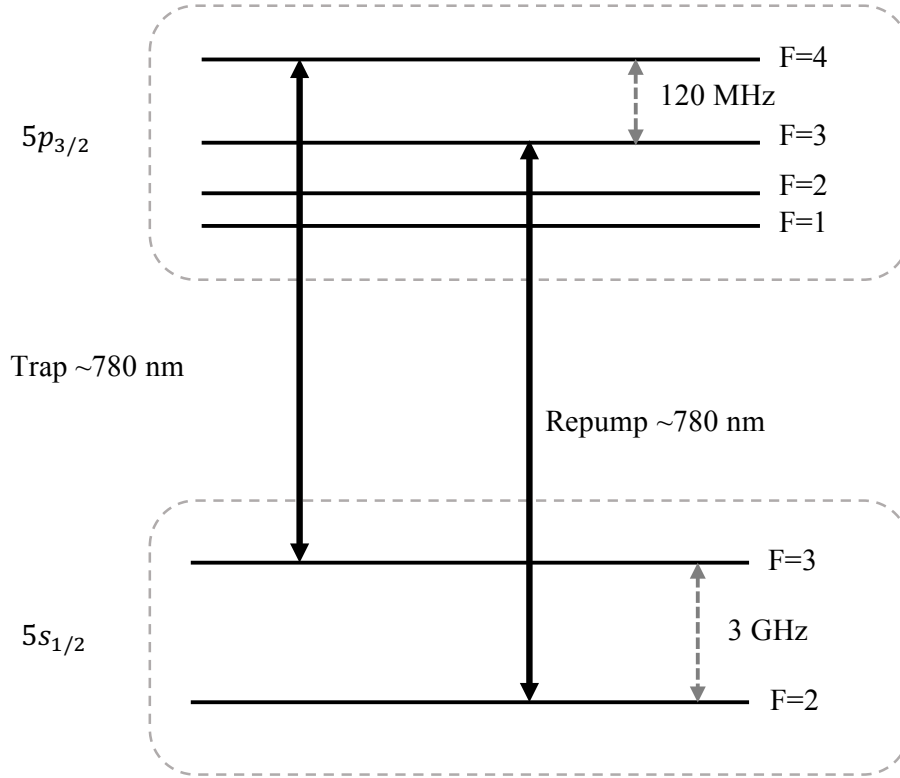


Figure 2.3: Hyperfine energy structure of  $^{85}\text{Rb}$ . Trap laser drives the transition,  $5s_{1/2}$   $F=3$  to  $5p_{3/2}$   $F=4$ , and the repump laser drives the transition,  $5s_{1/2}$   $F=2$  to  $5p_{3/2}$   $F=3$ .

### 2.1.2 Saturated Absorption Spectroscopy

To establish and maintain well-defined frequency for the trap laser and repump laser, the lasers are frequency locked using feedback from Saturated Absorption Spectroscopy or SAS. Our implementation of SAS is:

1. Split off a small fraction from the main beam of the laser, and direct it through a cell containing Rb vapor at room temperature. This beam is called the “pump” beam and it is sufficiently intense to saturate the Rb absorption along its path.
2. Retro-reflect the pump beam as the “probe” beam.
3. Detect the probe intensity using a photo detector. If the beam frequency is slightly detuned from resonance, due to Doppler effect, atoms in the cell will

absorb light from the pump or probe beams, respectively. If the beam frequency is tuned to resonance, only zero-velocity atoms can absorb photons from the pump beam. Since there are no additional zero-velocity atoms available to absorb photons from the probe, it passes through the cell unattenuated. Thus there is an intensity increase of the probe beam when the frequency of the beam is scanned over the resonance frequency.

In the experiment, the real setup is a little more complicated than the above description. The beam passing through the cell has been split further into two beams. One comes back as a probe and the other is detected directly. The detected signal from the probe is then subtracted by the signal from the other beam, enabling a differential measurement. In this way, we can get rid of the fluctuation of the main beam intensity and stabilize the absorption spectrum.

The SAS signal vs trap and repump laser frequencies are shown in Figure 2.4. These signals are generated by sweeping the grating piezo voltage of the external cavity diode lasers with a triangle or sine wave. They help us lock the laser frequencies, which are very easily to drift away in a very short time.

The peaks other than the marked transition peak shown in Figure 2.4 are called “crossover” peaks. They are generated by non-zero velocity atoms at mean frequency of each pair of the real hyperfine transition peaks. We use servo-loops to lock both trap and repump lasers to the side of a resonances. When locked, the saturated absorption signal is compared to zero volts and the error signal is feedback to the piezo. This is a negative feedback so that the lasers can be locked.

For the trap laser, the setpoint is usually placed in the middle of the crossover peak and the  $F=3$  to  $F=4$  resonance peak. The frequency gap between this setpoint and the  $F=3$  to  $F=4$  resonance peak is  $\sim 58$  MHz. In the lab, before the SAS beam has been sent to the

absorption cell, it has already been blue detuned by 36 MHz. So after the trap laser has been locked, it is red detuned by  $\sim 22$  MHz from the real  $F=3$  to  $F=4$  resonance. This red detuning value is the optimized value from daily operation.

For the repump laser, we find that the locking setpoint has a much higher tolerance than the trap laser. This is expected because the repump is dealing with small amount of atoms which are imperfectly transferred from  $F=2$  to  $F=3$  by the trap laser. So the red dotted arrow in Figure 2.4 gives an approximation setpoint to lock the frequency. The setpoint can be shifted somewhat and there is no significant change of the MOT fluoresce.

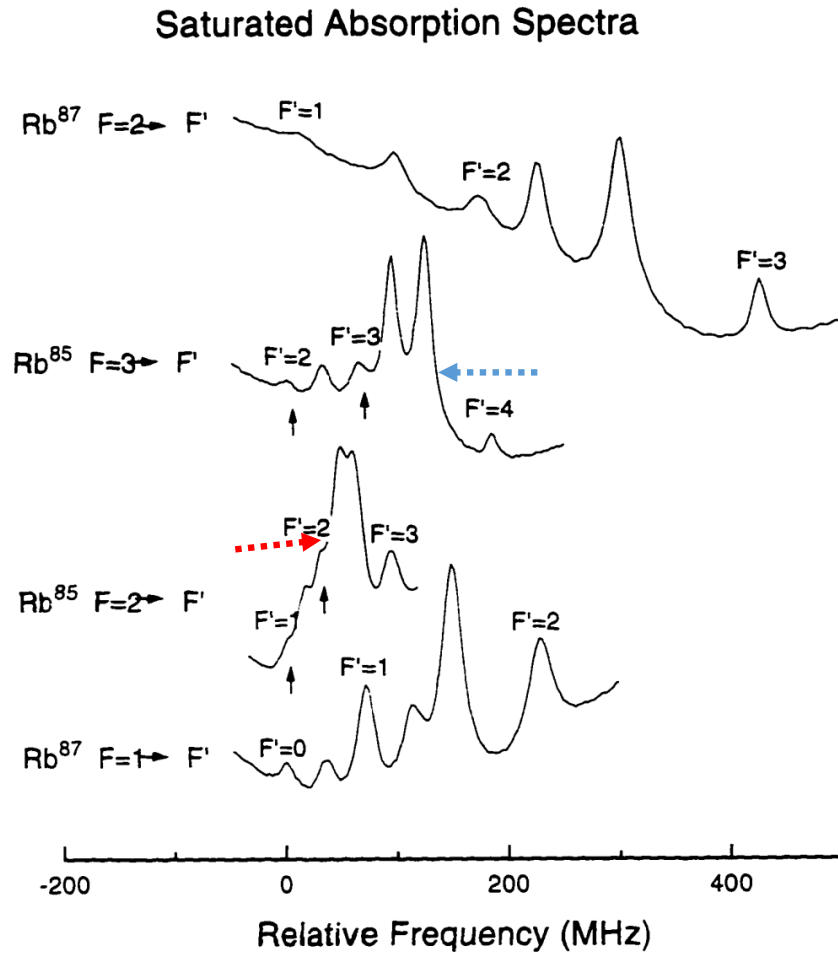


Figure 2.4: The saturated absorption spectra for the Rb  $5s_{1/2}$  to  $5p_{1/2}$  hyperfine transitions and their crossover peaks [3]. Small dark arrows are pointing to the real resonances. Blue

dotted arrow, pointing to the side of the crossover peak, indicates where the trap laser is actually locked at. Red dotted arrow indicates the position where the repump laser is locked at.

### 2.1.3 Ultra High Vacuum Chamber

At high pressures, the collisions with high speed atoms reduces the number of atoms collected and held in the trap. So an ultra high vacuum environment is necessary for the MOT. In our lab, the MOT is positioned inside an ultra high vacuum chamber, which is using an ion pump to maintain its ultra high vacuum.

The pressure in the UHV chamber can be measured by two types of gauges: thermocouple and Bayard-Alpert ionization gauges, both of which are monitored by Varian senTorr gauge. The thermocouple gauge measures pressure from  $10^{-3}$  to  $10^2$  torr. It is used during rough pumping process. The ion gauge can measure as low as  $2 \times 10^{-11}$  torr. Turning it on affects the MOT so we don't use it during experiment. We usually refer to the ion pump reading for daily operation. It provides an approximate reading. The usual operation pressure read from the ion pump is between  $10^{-9}$  torr to  $10^{-8}$  torr.

### 2.1.4 Characterization of the MOT

The temperature of the atoms trapped in the MOT can go down as low as about  $70 \mu\text{K}$ . Details on how the atom's temperature is measured are provided by Mary Kutteruf in [4].

To measure the density of the MOT, we use an optical imaging method. A CCD camera detects the fluoresce from the MOT. The detected signal is compared with the model

calibrated by Mary Kutteruf [4] and reveals the density of the MOT. The density range covers from orders of  $10^8 \text{ cm}^{-3}$  to orders of  $10^9 \text{ cm}^{-3}$  in our lab.

## 2.2 Lasers and Amplifiers

### 2.2.1 Nd:YAG Lasers

Nd:YAG lasers are solid state lasers. The lasing medium is neodymium-doped yttrium aluminum garnet ( $\text{Nd: Y}_3\text{Al}_5\text{O}_{12}$  or Nd: YAG). The medium is pumped by flash lamps and absorbs mostly in the bands between 730–760 nm and 790–820 nm [5]. It then emits light primarily centered at 1064 nm. For our pulsed Nd:YAG lasers, a Q-switch closes the optical cavity at the optimal time to extract maximal energy from the cavity following the pulsed flashlamp excitation [refer to Figure 2.6]. The infrared output is not very useful either for directly pumping dye lasers or exciting atoms in our experiments, but it can be used to generate beams of other frequencies. For the experiments described in later chapters, Potassium Dihydrogen Phosphate (KDP) crystals are used to generate 2<sup>nd</sup> or 3<sup>rd</sup> harmonics of the source frequency. 2<sup>nd</sup> and 3<sup>rd</sup> harmonic beams have wavelengths of 532 nm and 355 nm respectively. We use the green light at 532 nm from two different lasers to pump a regenerative Ti:Sapphire amplifier, a multi-pass Ti:Sapphire amplifier for THz generation and a dye laser for Rydberg excitation. The ultraviolet light at 355 nm is used to pump several dye amplifiers for Rydberg excitation.

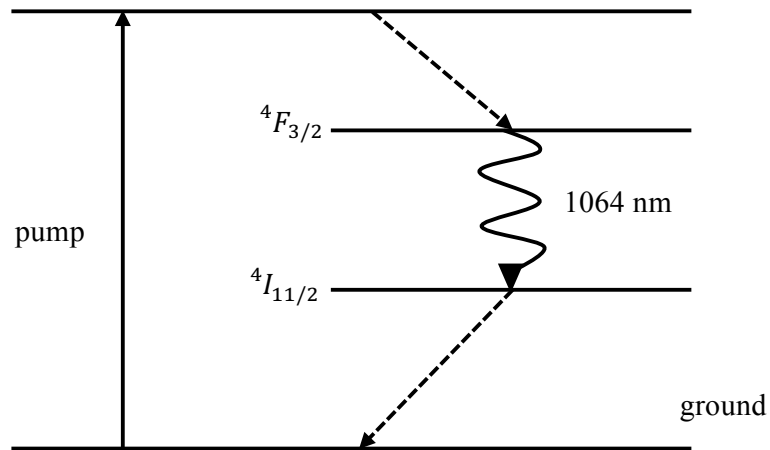
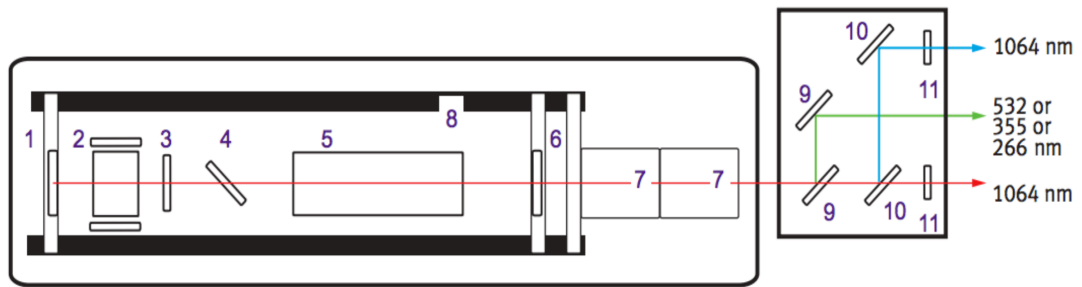


Figure 2.5: Schematic of Nd:YAG lasing [6]. It is a typical four-level lasing scheme.



1 Rear Mirror, 2 Pockels Cell, 3  $\lambda/4$  Plate, 4 Dielectric Polarizer, 5 Oscillator Rod, 6 Gaussian Output Coupler, 7 Optional Harmonic Generators, 8 Graphite Resonator Structure, 9 Dichroic Separation, 10 1064 nm Mirrors, 11 Beam Block

Figure 2.6: Layout of Continuum Surelite Nd:YAG laser. It can output beams of 4 different frequencies [5].

One Nd:YAG laser combined with KDP can generate 2<sup>nd</sup> and 3<sup>rd</sup> harmonics at the same time. But some measurements require 2<sup>nd</sup> and 3<sup>rd</sup> harmonic pulses at substantially different times. So two Nd:YAG lasers are used for the experiments. One is Spectra-Physics GCR-100 Series. Its function is to generate 532 nm green laser light. This green laser is the



pump for the regenerative amplifier and the multi-pass amplifier, both of which will be discussed later. The other Nd:YAG laser is Continuum Surelite. It is used to generate ultraviolet 355nm laser light, which is to pump dye lasers and dye amplifiers in the experiments. Both lasers produce pulses with durations of 5-10 ns and fire at 15 Hz repetition rate.

### 2.2.2 Diode Lasers

Diode lasers are lasers use a  $p-n$  junction or a  $p-i-n$  structure to generate gain. Semiconductor lasers are usually compact, efficient and inexpensive, so diode lasers are commonly used whenever possible. Another advantage of diode lasers is that their output frequency is tunable. The frequency of an external cavity in a diode laser can be controlled by tuning the angle of a small grating in the diode laser head using a piezo. The following diode lasers are used in the experiments.

- Vortex tunable continuous wave (CW) diode lasers from New Focus. Typical output frequency is 780 nm and output power 40 mW. They are used as trap and repump lasers for the Magneto-Optical Trap.
- TA-SHG pro high power frequency-doubled tunable diode laser system. Typical output frequency is  $\sim 490$  nm and output power 150 mW. It is used for Rydberg excitation.

### 2.2.3 Mode-Lock Laser

The mode-lock laser used in the experiments is model MTS mini Ti:Sapphire laser kit from KMLabs. It uses passive Kerr-lens mode-locking. Its diagram is shown in Figure 2.7. The cavity is designed to have lower loss for pulsed rather than CW operation. The shorter the pulse travels in the cavity, the higher the intensity, the greater the effect of Kerr-lensing

in the gain medium, and the lower the loss. The routine operation to initiate mode-locking is to displace one of the two prisms used for group velocity dispersion (GVD) compensation. The disturbance develops into a single short pulse oscillating in the cavity with durations as short as 15 fs at a repetition rate of  $\sim 90$  MHz. The output pulse spectrum is monitored using a spectrometer. If the output is not mode-locked, it is a CW beam and the spectrum is a line with no bandwidth. For well mode-locked pulses, the spectrum is very stable and has a large ( $\sim 50$  nm) bandwidth. The temporal narrowness of the output pulses is more than sufficient for our experiment but the pulse energy is much too small. To generate short pulses with large enough power, we use pulses from the mode-lock laser to “seed” an amplifier. The amplification process is discussed in 2.2.4.

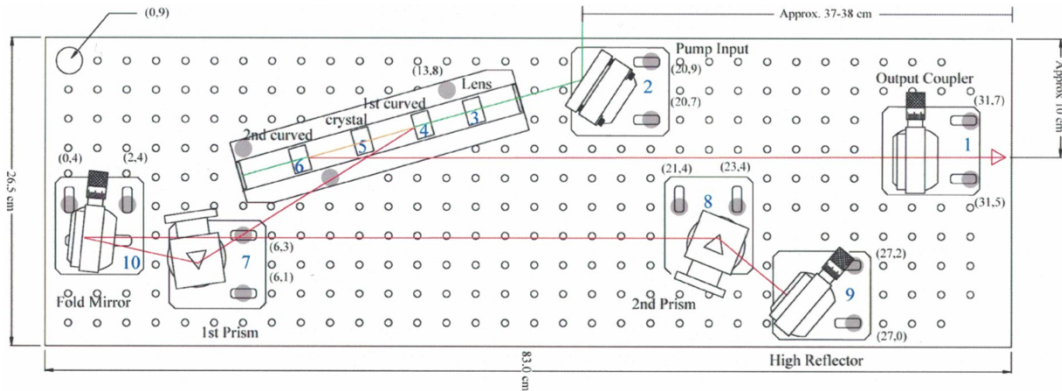


Figure 2.7: Basic layout of the mode-lock laser [12]. The green line is the pump light from Millennia Vs laser and the red line is the mode-locked beam in the cavity which is centered at 780-800 nm. The prism pair is used to compensate for group velocity dispersion (GVD). By tapping the 2<sup>nd</sup> prism, we can produce a temporary unstable beam. Stronger intensity part in this beam will be enhanced, producing the periodic pulsed output.

### 2.2.4 Chirped Pulse Amplification

As mentioned above, the output from the mode-locked laser has a very short duration but its amplitude is not large enough for the experiments. So pulses from the mode-lock laser, or the so called “seed light”, has to be amplified. This is achieved through a popular technology called “Chirped Pulse Amplification”. The basic idea is this:

1. Stretch the short pulses to a broad duration so that the peak intensity is not very high. As shown in Figure 2.8, the combination of reflecting mirrors, a grating and a lens in the stretcher acts as a pair of gratings and disperses the seed light’s spectrum. In the stretcher, the low-frequency component of the laser pulse travels a shorter path than the high-frequency component does. So after the stretcher, the pulse is “chirped” and the duration is thousands times longer than the original.
2. Amplify the stretched pulses using amplifiers such as regenerative amplifiers and linear amplifiers. Since the pulse duration is long, the peak intensity is relatively small so that it does not damage the optics.
3. Compress the amplified stretched pulses to high intensity short pulses using a compressor. The compressor acts as the inverse of a stretcher, and it also utilizes a grating. In the experiments, the compressor is adjusted to optimize the non-linear Thz generation for experiments.

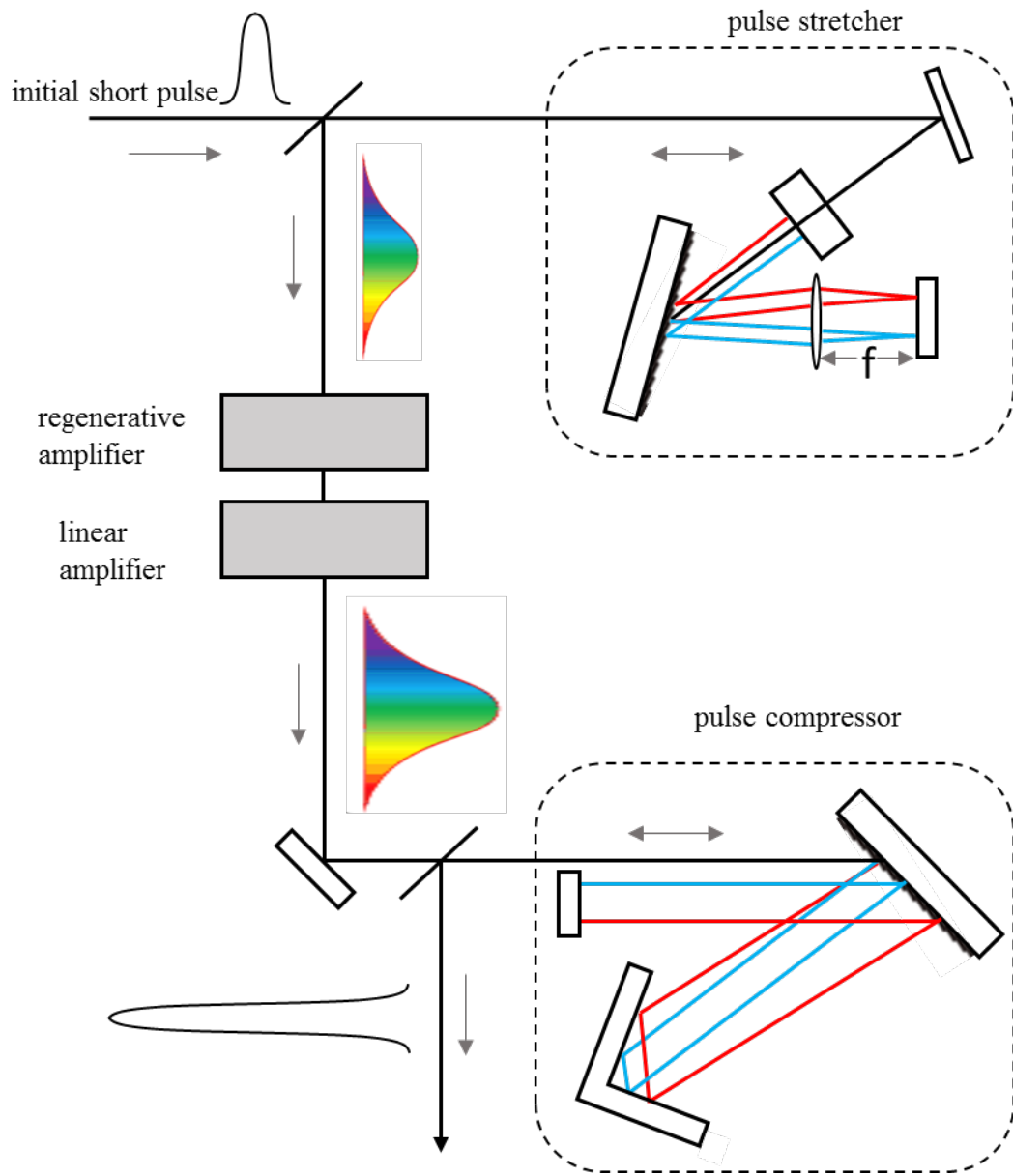


Figure 2.8: Schematic of chirped pulse amplification system. Seed light is first temporally stretched using the stretcher. Then the stretched pulse gets amplified. Finally the pulse is again compressed to something close to its original duration, but with much greater ( $10^6 - 10^7$  times) energy.

### 2.2.5 Regenerative Amplifier

The first amplifier in the chirped pulse amplification is a regenerative amplifier. It uses Ti:Sapphire as the gain medium. The schematic is shown in Figure 2.9. A fast pick-up pockels cell cooperating with a polarizer, picks up a single pulse from the seed light before sending it into the regenerative amplifier. The input pulse has a vertical polarization to the paper surface and can be reflected by the first polarizer to the switch-in pockels cell. The switch-in pockels cell has a high voltage applied on it. It works as a quarter waveplate and rotates the pulse's polarization from vertical to horizontal before it comes back to the first polarizer. As soon as the pulse changes the polarization to horizontal, the switch-in pockels cell is triggered off and does not affect the pulse's polarization during the pulse's journey in the cavity. Now the switch-in pockels cell is also blocking some leakage pulses from the pick-up pockels cell out of the cavity. The switched in pulse with horizontal polarization goes through the first polarizer and comes into the gain medium to get amplified. It then goes through the switch-out pockels cell, which is off, and is then reflected back to the cavity. After multiple runs (usually 20 runs) in the cavity to gain maximum intensity, the switch-out pockels cell is triggered on and the pulse is switched out with a vertical polarization.

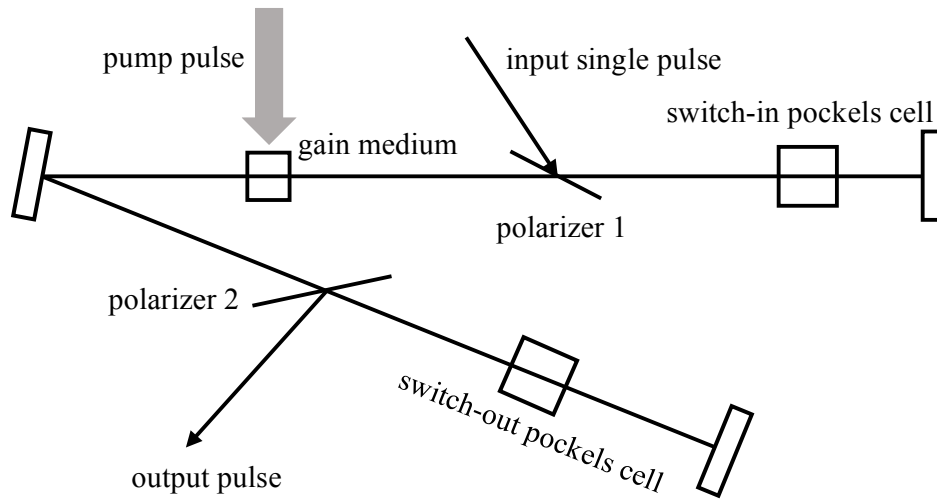


Figure 2.9: Schematic of regenerative amplifier. The switch-in pockels cell controls when a seed pulse is trapped in the resonator and the switch-out pockels cell controls when the pulse is ejected from the cavity.

### 2.2.6 Linear Amplifier

An additional multi-pass amplifier is used when the pulse energy from the regenerative amplifier ( $\approx 3$  mJ) is not large enough for the experiments. The pulse obtains additional amplification by making three passes through another Nd:YAG laser pumped Ti:Sapphire crystal. The highest output from the linear amplifier in our lab is over 40 mJ (prior to the compressor). It is shown structurally in Figure 2.10.

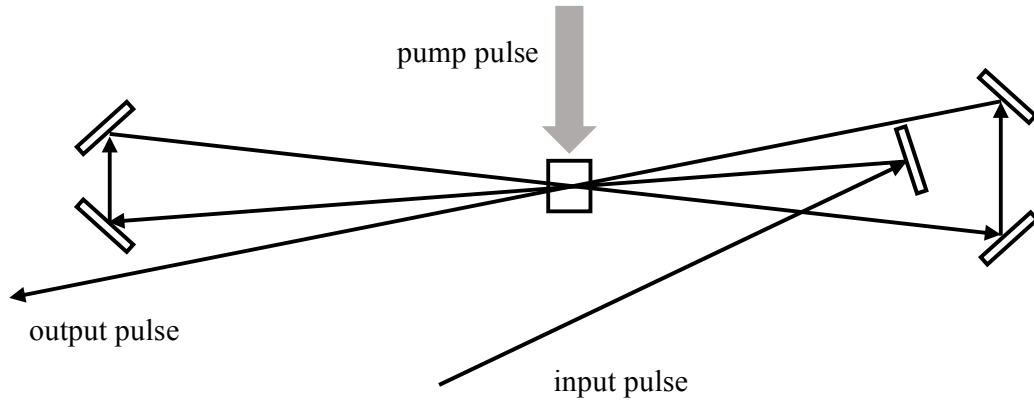


Figure 2.10: Schematic of linear amplifier. The beam passes the Nd:YAG pumped gain medium three times and gets amplified.

### 2.2.7 Dye Laser and Dye Amplifier

In our experiments, a Hansch-style dye laser [7] has been used for Rydberg excitations. This dye laser is used to generate  $25s$  Rydberg atoms. The proper laser dye is LDS 925, which is dissolved in methanol solvent, with a concentration of 250 mg/L. This solution is pumped by the 2<sup>nd</sup> harmonic from Continuum Surelite. The pump light has been focused about a millimeter into the dye cell by a cylindrical lens, creating a line of gain medium across the face of the cell. The dye cell works as a fluorescence generator, as well as an amplifier. The telescope expands and collimates the beam. The grating is rotatable, which determines the frequency of the light diffracted back to the cavity.

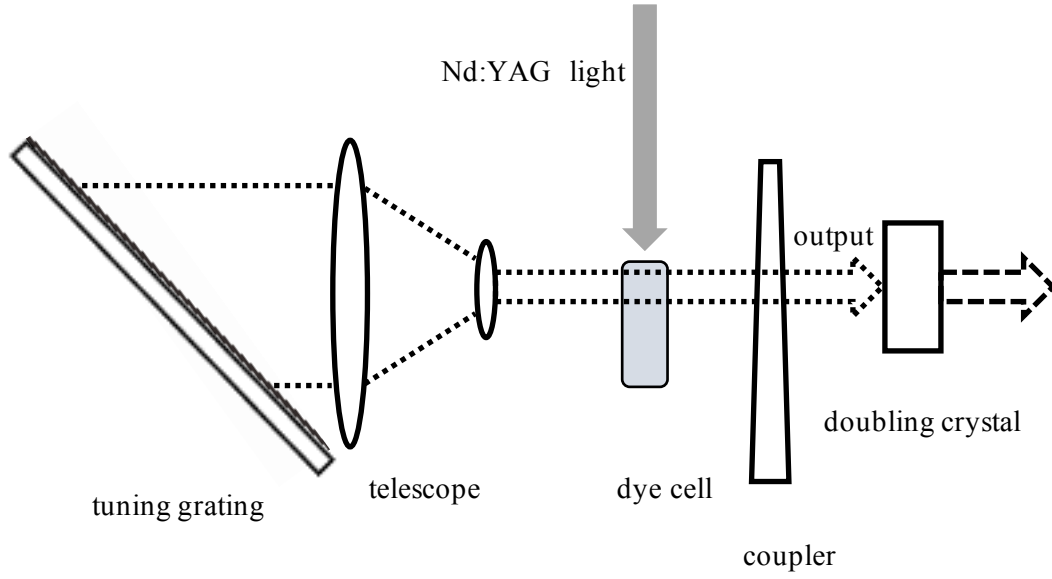


Figure 2.11: Schematic for a Hansch dye laser and the 2<sup>nd</sup> harmonic generation. The angle of the tuning grating determines the output frequency.

The infrared ( $\sim 970$  nm) output of this laser is then frequency doubled to generate blue laser pulses at 486 nm. The output beam from the doubling crystal has a electric field  $E(2\omega) \sim \chi_2 E(\omega)E(\omega)$ , where  $\chi_2$  is the 2<sup>nd</sup> nonlinear susceptibility tensor and  $E(\omega)$  is the electric field of input beam. So the frequency doubled pulse has a narrower line width than the original pulse. A typical line width is on the order of  $1 \text{ cm}^{-1}$ . The rough tuning of the frequency is accomplished by the grating inside the laser. The fine tuning is accomplished by putting an etalon (1 mm thickness) after the doubling crystal and changing its angle. The output from the etalon is then saturated by a dye amplifier. A dye laser is usually very unstable in intensity from shot to shot. The saturation amplified can reduce the fluctuation between shots. The amplified beam is then sent to the chamber, and drives Rb atoms from  $5p$  state to  $25s$  state.



A flowing dye cell without cavities serves as an amplifier as shown in Figure 2.12. The double amplifier shown is used to amplify laser pulses from dye or diode lasers. Before taking measurements, we have to make sure the transition has been saturated by the amplified beams. If there is no significant reduction of the Rydberg population on a state (e.g, 25s) when an 80% transmission filter is inserted in the beam path, we are confident that the state transition is saturated.

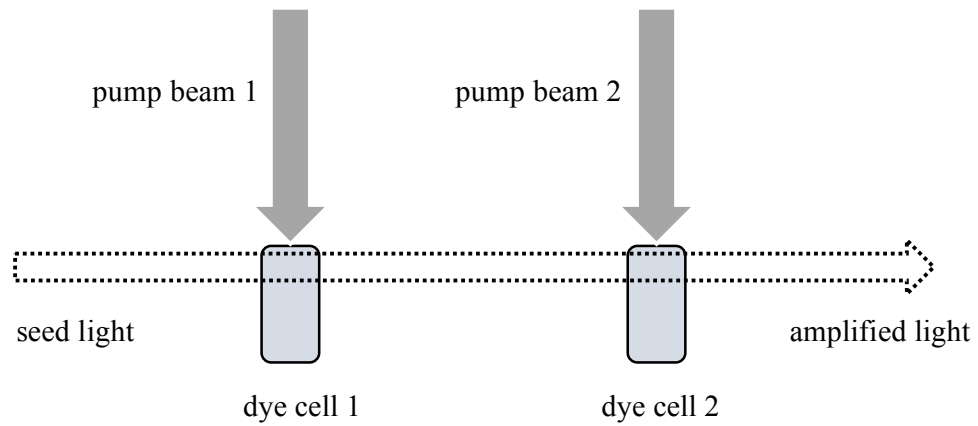


Figure 2.12: Schematic for double cell dye amplifier used in the lab.

## 2.3 THz Pulses

The duration of the THz pulses generated in our lab is on the order of a few ps (a typical THz pulse generated in the lab is shown in Figure 2.13). The THz pulses can coherently redistribute Rydberg population on time scales that are negligible compared to the relatively long time required for other interactions (such as Dipole-Dipole interactions). So we use THz pulses to induce and probe coherent population distribution in the experiments described in chapters 5 and 6. The THz setup for experiments in this dissertation follows that developed by Sha Li for her research. For a detailed discussion of THz generation and

characterization, one can refer to her dissertation [8]. A brief introduction of THz generation will be provided in this chapter.

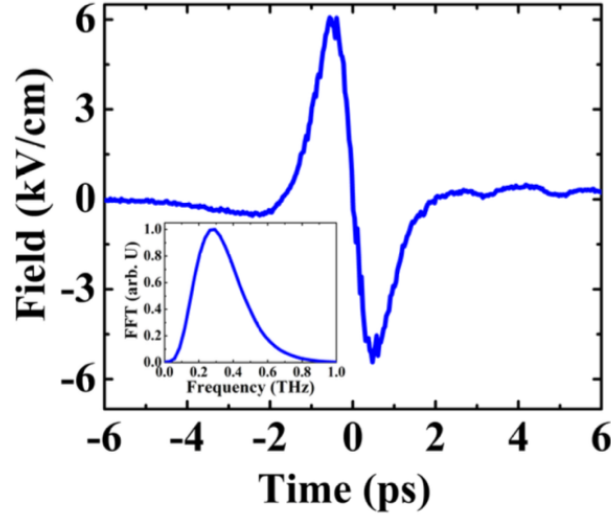


Figure 2.13: A typical THz pulse generated in the lab [8]. The duration is about 5 ps and the peak frequency is 0.2-0.4 THz. This pulse is generated using tilted-pulse-front-pumping optical rectification and the temporal profile of the pulse is characterized using the electro-optic sampling method. The frequency spectrum is then derived from the time-domain profile.

The THz pulses used in the experiments are generated via tilted-pulse-front-pumping (TPFP) optical rectification of femtosecond laser pulses in a LiNbO<sub>3</sub> crystal. It utilizes the so called difference frequency generation (DFG) phenomenon and is actually a cascaded intrapulse DFG [9]. When an ultrafast laser pulse (broad bandwidth) pass through a nonlinear crystal with non-vanishing  $\chi_2$ , it creates a polarization that follows the intensity envelope of the pump field. The induced polarization is a source of electromagnetic radiation. The frequency bandwidth of our femtosecond pulses lies in THz regime (e.g. a sinusoidal pulse with Gaussian envelope,  $\Delta\tau_{FWHM} = 100$  fs has a bandwidth of  $\Delta f_{FWHM} =$

4.41 THz), thus optical rectification of ultrafast femtosecond laser pulses can be used to generate THz radiation.

Efficient nonlinear conversion requires phase matching. Hebling et al. proposed a tilted-pulse-front-pumping scheme for phase matching [10]. In the TFP scheme, the intensity front of the near-infrared (NIR) pump pulse is tilted by an angle of  $\gamma$  inside the crystal via grating diffraction, and the crystal is cut at this angle to obtain a beam exiting normal to the crystal surface. As shown in Figure 2.14, when  $v_{NIR}^{gr} \cdot \cos\gamma = v_{THz}$ , where  $v_{NIR}^{gr}$  is the group velocity of near-infrared light beam in the crystal, the propagation direction of the generated THz radiation is perpendicular to the intensity front of the pump.

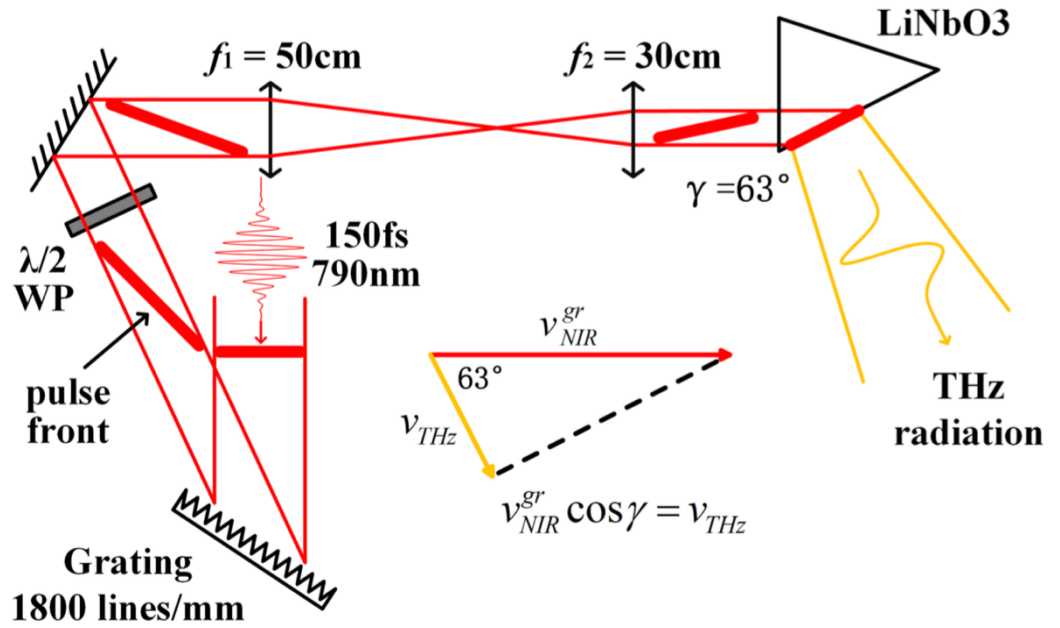


Figure 2.14: Schematic of TFP setup [8].

## 2.4 Detection and Data Collection

### 2.4.1 State-Selective Field Ionization

As an efficient state distribution detection technology, State-Selective Field Ionization (SSFI) has been used widely to measure the state distribution of atoms [11].

In alkali atoms, the outermost electron is bound in a potential trap that has the form,  $V(r) \sim 1/r$ . When a static field is applied to the atom, the potential tips to one side as shown in Figure 2.15. This lowers the barrier that traps the electron. When the barrier is low enough, the electron is able to escape from the trap. During the tipping process in a rising field, higher energy electrons tend to be ionized sooner than low energy electrons, so that the probability that the atom was in a state with a particular principal and (perhaps) angular momentum quantum number is proportional to the ionization signal at a particular time.

In the MOT chamber, there are four metal rods. Two of them are connected to a high voltage pulse supply and the other two are connected to ground or low static voltage. Pulsed voltages applied to these 4 rods create strong electric fields with 1  $\mu s$  (slow ionization field) or 500 ns (fast ionization field) rise times. Atoms in the field will be ionized and the ions will fly in the ionization field toward a detector composed of micro-channel plates (MCP). Atoms in different states are ionized at different times, so the electric signal have different arrival time thus the population of states can be distinguished.

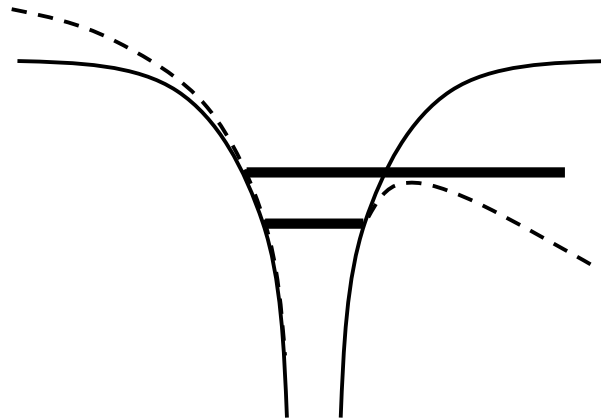


Figure 2.15: Schematic of the tipping of electron potential. Solid line is the  $1/r$  potential when there is no external field applied to the atom. Dashed line shows the tip of potential when a field is applied to the atom. When such a field is strong enough, electrons are able to escape from the trap.

### 2.4.2 Synchronization System

Before taking any measurement, various lasers and electric field pulses must be synchronized. The synchronization is controlled by a timing system in the lab. It introduces a combination of clocks, delay generators and synchronization boxes. The principal behind the system is that it is flexible enough to adapt to changes. Figure 2.16 shows the synchronization system working in the experiment described in Chapter 6. Small changes are needed to use this system to work for other experiments. The “master” clock is a divider which divides the commercial 60 Hz electrical supply by 4 and provides a 15 Hz source to trigger a multi-channel digital delay/pulse generator, Model DG535 from Stanford Research Systems. One channel of this delay generator triggers a second DG535 which controls the firing of the lamps inside the Surelite Nd:YAG laser. Another channel triggers

the lamp of GCR-100 Nd:YAG laser. The GCR-100 provides a “ready” signal at the optimal time for firing Q-switch. This Q-switch request signal is delayed by up to one period of the mode-locked pulse train from the Ti:Sapphire oscillator in the SM-1 synchronization box. The SM-1 is synchronized with the mode-locked pulse train and triggers the GCR-100 Q-switch as well as two additional digital delay generators (a DG535 and a DG645). The DG535 controls pockels cells in the regenerative amplifier. The DG645 controls the Q-switch of the Surelite Nd:YAG, and triggers the ionization field, oscilloscopes and etc. The delays are easy to change on these delay generators so this system can handle different timing for different experiments.

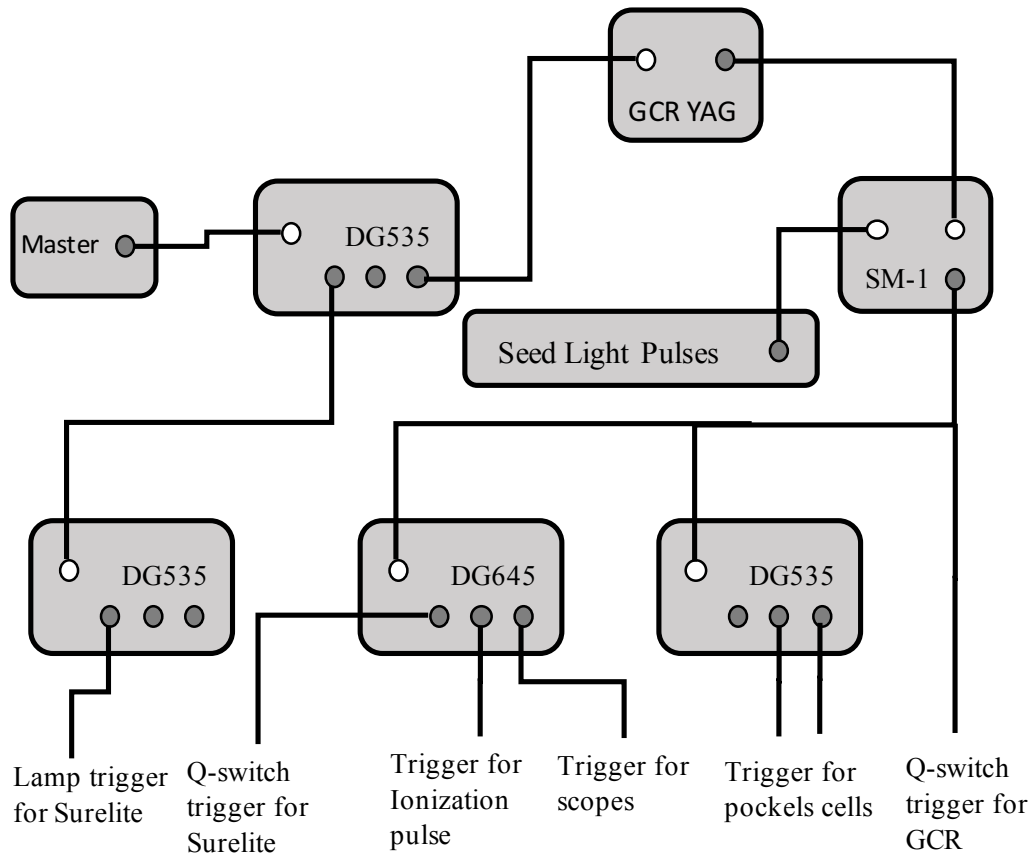


Figure 2.16: Schematic of the synchronization system. White circles are inputs and dark circles are outputs.

### 2.4.3 Measurement Operation

The time-dependent ionization signal from the MCP detector is collected using oscilloscopes, and the oscilloscopes transfer the data to computers via data collection programs written in Labview. A typical electric signal representing a state population is a peak with some width. Usually, the larger a state population is, the higher the peak is. But the height alone is not an accurate measure of the population. Instead, the area of peak is proportional to the state population. As shown in Figure 2.17, the peak within the temporal gate or window is the ionization signal associated with particular states. Using the Labview code, we can record the area under the peak in the user defined gates on each laser shot. After subtracting this area by the area when there is no ionization, we obtain the Rydberg population. As the population changes, the integrated value in the gate changes accordingly.

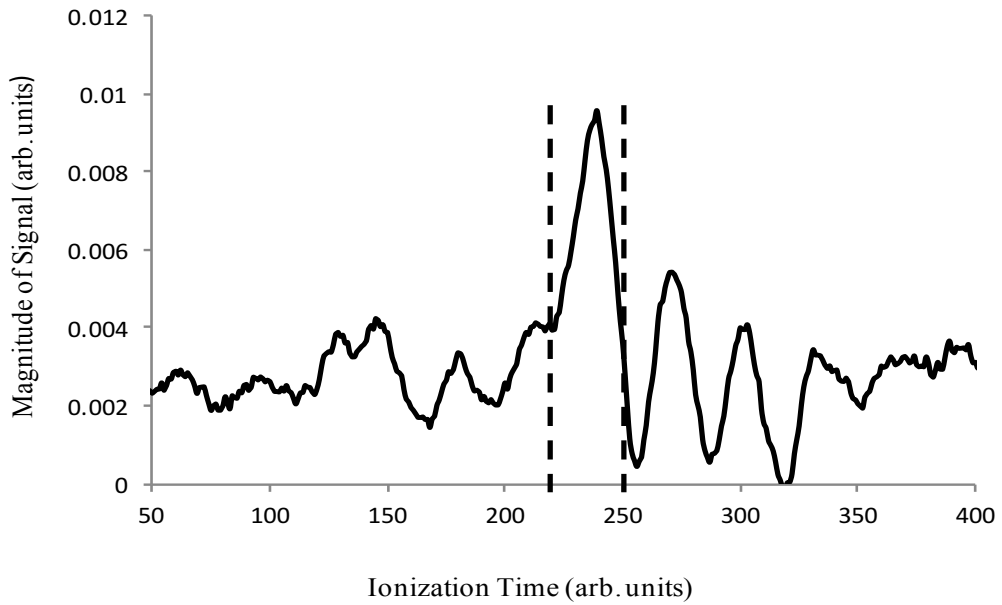


Figure 2.17: A typical ionization signal shown on an oscilloscope. The central peak representing the population of state  $32s + 32p$ . The measurement program uses a user defined gate and integrates the area under the peak within the gate.

## 2.5 Maintenance and Daily Operation

Before doing experiments, participants must have finished the safety training.

Before turning on lasers, the laboratory main interlock switch has to be flipped on. It enables the lasers in the lab. When the switch is on, a red light bulb outside the lab is illuminated to indicate “laser on” status.

### 2.5.1 Daily Examination

1. Check the MOT chamber pressure. The reading from the ion pump should be no more than orders of  $10^{-8}$  torr. If the pressure is higher than this reading, there might be some leakage.
2. Check pressure of canned nitrogen which is used to keep GCR-100 laser head clean and dry. The inner pressure should be higher than zero and the output pressure should be around 5 psi. From previous experience, the nitrogen needs to be replaced every two to three weeks.
3. Check the room temperature readings. The readings should be from 72 °F to 74 °F. On some days, the temperature may be out of this range.
4. Check temperature of cooling water from external sources. The supply water should have a temperature around 60 °F.
5. Check cooling water level for each laser before turning on the laser. The water level should be in the proper range marked in the box.
6. Check the fume hoods to make sure they are working properly.



### 2.5.2 Operation of Regenerative Amplifier

Turn on the seed light pump laser power switch. When the temperature is stabilized, turn on the laser. The pump should be in mode “power” and the setup for power is “3.75 W” shown on the display screen.

1. Let the pump laser warm for at least half an hour. Then lock the mode. If the mode-lock is not very stable, usually it's because the alignment is off and it needs adjustment.
2. Turn on the regenerative pump GCR-100 Nd:YAG laser. Slowly increase the power of the pumping lamp until it reaches the maximum. It usually takes several seconds or minutes for the simmer light to turn on. If it takes too long, it's probably because there are too many ions in the cooling system and the charge of lamps is not working properly. Reflush the cooling system using deionized water if that happens and try again.
3. Let the Nd:YAG laser warm for at least one hour to acquire thermal balance.
4. Change the output pockels cell's timing to be the long timing set, which is 4 $\mu$ s longer than the short timing set (which should be almost the same every day). This is to enable self lasing of the amplifier. Switch on all the pockels cells in the setup. Increase the Nd:YAG pump light to be a little higher than the threshold. (The threshold may vary a little bit every day. The recent value should be marked down in the log book.)
5. There should be a bright spot showing in the TV monitor, which means the regenerative amplifier is now lasing itself. If there is no bright spot, increase the pump light a little higher but not larger than the normal pump level. Adjust the coupling mirrors to make sure the threshold is minimized.
6. Block the pump light. Change back the output pockels cell's timing to the short timing setting. Increase the pump light to the ordinary operation level (which is also written down in the log book). Unblock the pump light. Now on the scope, there should be a

stably increasing pulse train, as observed on the photodiode detecting the light leakage through the regenerative amplifier cavity mirror.

At this point, the regenerative amplifier is ready. Fine tuning includes decreasing the threshold and making the pulse train more stable. The lamps in the Nd:YAG laser must be replaced every 700 hours or so under current repetition frequency. The normal output and the last replacement date are marked underneath the laser head on the optical table.

### 2.5.3 Operation of the MOT

The MOT is very sensitive to external perturbations. So during experiments, try not to make large noises or vibrations.

1. First turn on the cooling water valves. Check the flow meter to make sure cold water is flowing through the MOT coils' cooling tubes. If there is no flow or the flow is too slow, the power supply for the main anti-Helmholtz coils should not be turned on. Check the paddle wheel monitor to make sure water can flow. The normal input pressure is 14 psi. Make sure there is no leakage of water from the cooling tubes.
2. Turn on diode lasers for the trap and repump beams.
3. Turn on the AOM driver, voltage ramp for the diode grating, scopes, TV monitors and coil power supply. Increase the output of the power supply of the main coils to 10V. The resistance of the main coils is 1 ohm, so the output current of the power supply should be around 10A.
4. Turn on the getter and slowly increase it to the operating value. A normal operating current is from 1.9 A to 2.5 A. When this value has to be as large as 3.5 A to generate an observable MOT on the TV monitor, it means the getter has been used up. Under ordinary usage, this process could take about 4 to 5 years. Once the getter has been used up, it should be replaced by a new one.

5. Let the trap and repump lasers warm for at least one hour to achieve thermal balance.

Then adjust the piezo voltage of the lasers to find the right absorption signal. If the absorption signal is no way similar to the proper pattern, use a spectrometer to check the output frequency. For the trap laser, the output frequency range should cover the value 384232.6 GHz and for the repump laser 384231.2 GHz. If either diode laser can reach the required value, it is possible that the piezo in the laser head is damaged and needs to be replaced. Lock lasers.

At this point, there should be a bright spot shown on the TV monitors. It is the scattered infrared light from the cold atoms. A good MOT on the screen is a bright stable spot with a clear circular shape. If the spot is not stable or the shape is not round, the first step to try is to adjust the current of the shim coils to make it good. If the shim coils do not do the job, usually it is because the alignment of the trap beams needs to be adjusted. Follow these troubleshooting procedures (refer to Figure 2.18):

1. Check the two windows for beams A and B respectively at the bottom of the chamber.

There should be a mask on each window. These masks make the trap beams well structured.

2. There are four additional masks, two are big and two are small, which help to align the trap beams. Attach two big masks to the front and the back windows, and adjust mirrors to make sure the trap beam C can go through the centers of the masks and be retro-reflected through them. Attach the two smaller ones to the top windows for beams A and B respectively. Make sure the beams' centers are the same as the masks' centers. Adjust mirrors so that beams A and B can come back along the same incoming paths. They should not totally overlap the incoming beams or the retro-reflected beams may be sent back to the trap laser head, causing unnecessary trouble.

3. Take off the masks. Turn on the switch which swiftly flips on and off the main magnetic field. If the fluoresce signal is not a round spot but with an irregular shape with one or more “tails”, which indicate the directions the atoms in the MOT tend to escape, adjust the shim coils and the mirrors to get rid of these “tails”.
4. Turn off the magnetic field switch. Now the MOT signal monitored by the camera should be a bright spot. If it is still not very steady or has blurry edges, fine tune the current of shim coils to make it better.
5. Adjust the repump beam to find the best performance of the MOT. The repump alignment does not affect the MOT much, so this step is not taken very often.

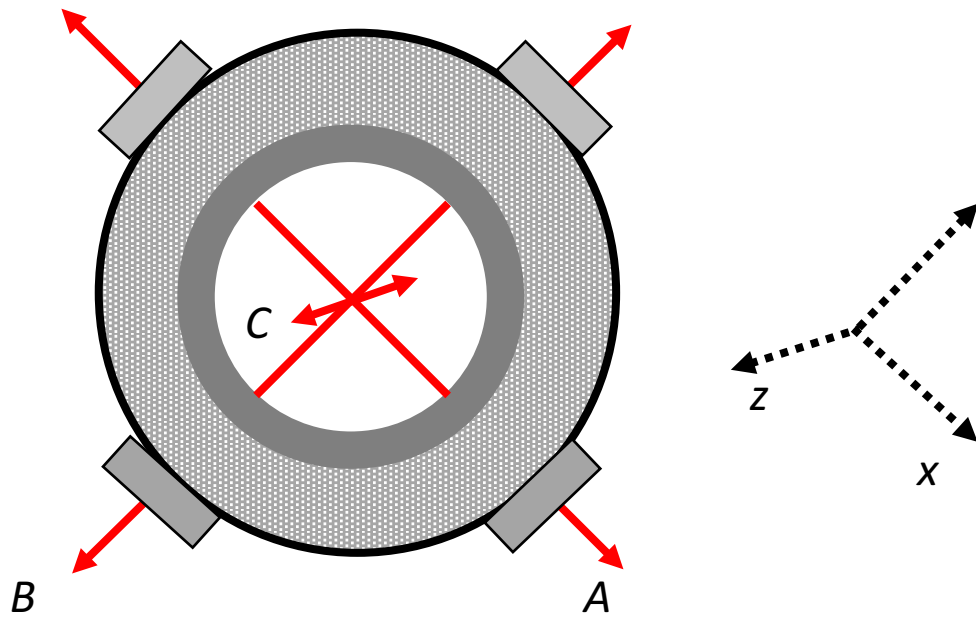


Figure 2.18: Front view of the chamber where the MOT is positioned in. A, B, and C represent three trap beams.

# Bibliography

- [1] E. L. Raab, M. Prentiss, Alex Cable, Steven Chu, and D. E. Pritchard. Trapping of Neutral Sodium Atoms with Radiation Pressure. *Phys. Rev. Lett.* 59, 2631 (1987).
- [2] Harold J. Metcalfe and Peter van der Straten. *Laser Cooling and Trapping*. Springer (1999).
- [3] W. Anderson, PhD thesis, University of Virginia (1996).
- [4] Mary Kutteruf, *Coherence in Rydberg Atoms: Measurement and Control*, PhD thesis, University of Virginia (2010).
- [5] Continuum, Mountain View, CA. *Operation and Maintenance Manual for SureLite Lasers* (1997).
- [6] Spectra-Physics, Mountain View, CA. *Pulsed ND:YAG Lasers User's Manual GCR-100 Series GCR-200 Series* (1993).
- [7] T.W. Hansch. Repetitively Pulsed Tunable Dye Laser for High Resolution Spectroscopy. *Applied Optics*, 11:895 (1972).
- [8] Sha Li, *THz Induced Field Ionization and Field Emission*, PhD thesis, University of Virginia (2016).
- [9] Mukesh Jewariya, Masaya Nagai, and Koichiro Tanaka. Enhancement of Tera-hertz Wave Generation by Cascaded  $\chi^2$  Processes in  $\text{LiNbO}_3$ . *J. Opt. Soc. Am. B*, 26, 9 (2009).
- [10] János Hebling, Gábor Almási, Ida Z. Kozma, and Jürgen Kuhl. Velocity Matching by Pulse Front Tilting for Large-area Thz-pulse Generation. *Opt. Express*, 10, 21 (2002).
- [11] Thomas F. Gallagher. *Rydberg Atoms*. Cambridge University Press (1994).

- [12] Kapteyn-Murnane Laboratory Inc, Model MTS Mini Ti:Sapphire Laser Kit Instruction Manual (2003).

## 3 Models in Simulation

This chapter introduces general knowledge about the physical models used in the research. The topics include Rydberg atoms, a two-body model, a dipole-dipole interaction model, blackbody radiation, etc. The mathematical equations presented provides a background for the simulations implemented in chapters 4, 5 and 6. Unless specifically noted, atomic units are used throughout this chapter.

### 3.1 Rydberg Atoms

Back to 1885, Balmer found the wavelengths of the visible series of atomic H is given by [1]:

$$\lambda = \frac{bn^2}{n^2 - 4} \quad (3.1)$$

where  $b = 3464.6 \text{ \AA}$ . We now know equation (3.1) is the formula for the wavelengths of the Balmer series of transitions from the  $n = 2$  states to the higher lying levels.

After quantitatively describing the wavelengths from H, people started to work on other atoms to unravel the mystery of atomic spectroscopy. Living and Dewar found that the observed spectral lines of Na could be grouped into different series [2]. Hartley found the significance of describing Balmer's formula in terms of the wavenumber or frequency of the observed lines instead of the wavelength during his reach on spectra of Mg, Zn, and Cd [3]:

$$\nu = \frac{1}{4b} \left( \frac{1}{4} - \frac{1}{n^2} \right). \quad (3.2)$$

This equation makes it more clear that the lines Balmer discovered reflect the energy differences between the  $n = 2$  and higher lying levels.

Following those pioneering measurements, Rydberg began to classify the spectra of other atoms, notably alkali atoms, into sharp, principal, and diffuse series of lines [4]. For example, he found the frequencies associated with transitions between the  $s$  and  $p$  series, are given by:

$$\pm \nu = \frac{Ry}{(m - \delta_s)^2} - \frac{Ry}{(n - \delta_p)^2} \quad (3.3)$$



where the  $+$  sign and constant  $n$  describe sharp transitions involving series of  $s$  states, and the minus sign and a constant  $m$  describe transition involving the principal series of  $p$  states. If  $\delta_s = \delta_p = 0$  and  $m = 2$  we can get Balmer's formula for the H transition from  $n = 2$ .

Due to his significant contribution, people now refer atoms in states of high principal quantum number as "Rydberg Atoms".

### 3.1.1 Modern Picture of Rydberg Atoms

If we consider Rydberg states of H and Na, as shown in Figure 3.1, they are quite similar. The only difference is that Na atom has a core which is composed of 11 positive charges and 10 electrons. In classical terms, at most of times, the high energy Rydberg electron is far from the core, where the difference between Na, H and all Rydberg atoms is trivial. But when the Rydberg electron comes near the core, it can both polarize and penetrate the  $\text{Na}^+$  core, altering the wavefunctions and energies of Na Rydberg states relative to their hydrogenic counterparts.

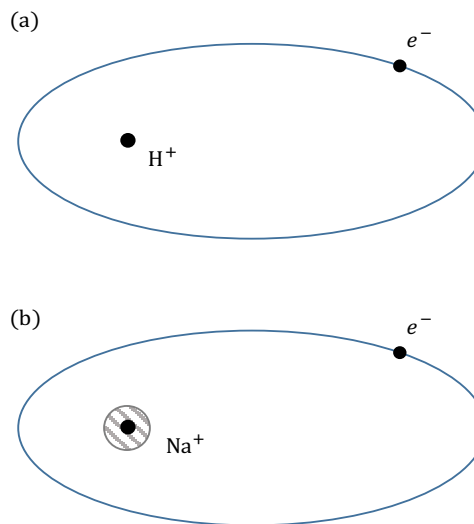


Figure 3.1: Classical view of Rydberg orbits of (a) H and (b) Na. In H the electron orbits around the proton. In Na it orbits around the  $+11$  nuclear charge and ten inner shell electrons.

In high  $L$  states Na behaves nearly identically to H, but in low  $L$  states the Na electron penetrates and polarizes the inner shell electrons of the  $\text{Na}^+$  core [5].

We know how to calculate wavefunctions of H [6]. This process can be easily extended to generate wavefunctions for single valence electron atoms with spherical ionic cores. Such an approach is called Quantum Defect Theory [7]. Quantum Defect Theory (QDT) assumes that the  $\text{Na}^+$  core is spherically symmetric and frozen in place. So the effective potential,  $V_{\text{Na}}$  seen by the valence electron is spherically symmetric and only depends on  $r$ . This potential is lower than the coulomb  $-1/r$  potential only at small  $r$ , and the effect is to increase the electron's kinetic energy and decrease the wavelength of the radial oscillations relative to H. In general, the bound state radial wavefunctions are given by:

$$\rho(r) = f(W, l, r)\cos\tau - g(W, l, r)\sin\tau \quad (3.4)$$

where  $f(W, l, r)$  and  $g(W, l, r)$  are commonly termed the regular and irregular coulomb functions and  $\tau$  is the phase shift which is related to the quantum defect,  $\delta_l$ . For a give principal quantum number, the Rydberg atom has allowed eigen energies:

$$W_n = -\frac{1}{2(n - \delta_l)^2} \quad (3.5)$$

where  $n$  is an integer. Equation (3.5) can be used to calculate the energies of Rydberg atoms if the quantum defects  $\delta_l$  are known. Table 3.1 gives the 0<sup>th</sup> order approximation of the quantum defects for Rb.

	$s_{1/2}$	$p_{1/2}$	$p_{3/2}$	$d_{3/2,5/2}$	$f_{5/2,7/2}$
$\delta_l$	3.13109	2.65456	2.64145	1.347157	0.016312

Table 3.1: Quantum defects for low- $\ell$  states of Rb [5].

From Table 3.1 we see that, for larger  $\ell$ , the quantum defect is smaller. This is to be expected as the centrifugal barrier reduces the probability of finding the electron near the nucleus as  $\ell$  increases.

### 3.1.2 Properties of Rydberg Atoms

Table 3.2 summarizes the dependence on principal quantum number  $n$  of some properties of Rydberg atoms [11].

property	$n$ dependences
Binding energy	$n^{-2}$
Energy between adjacent $n$ states	$n^{-3}$
Orbital radius	$n^2$
Orbital period	$n^3$
Geometric cross section	$n^4$
Dipole moment $\langle ns er np\rangle$	$n^2$
Polarizability	$n^7$
Radiative lifetime	$n^3$
Fine-structure interval	$n^{-3}$

Table 3.2: Properties of Rydberg Atoms.

Because the Rydberg wavefunction extends far from the ion core, they are easily affected by external fields, including those created by other atoms. For example, as introduced in later sections, the magnitude of dipole-dipole interaction between Rydberg atoms is proportional to the product of two transition dipole moments and, therefore, scales

as  $n^4$  for atoms in states of similar  $n$ . In addition, the very long lifetime of Rydberg atoms makes it possible to perform complex control operations on the the atoms prior to their decay. These superior properties make them ideal objects for researching coherent dipole-dipole interactions and the control of electron dynamics.

## 3.2 Two-Body Model

### 3.2.1 Introduction to the Two-Body Model

When talking about the interactions (which will be introduced in detail in 3.3) between atoms, a simplified two-body dipole-dipole (DD) model is often used. In this model, we suppose one atom is only affected by its nearest neighbor. Such an assumption is not completely accurate of course, because nearest neighbor interactions do not preclude the influence from other atoms. However, due to the inverse cube dependence of the DD coupling on atom separation, nearest neighbor interactions are typically several times larger than the next-nearest neighbor couplings. Moreover, compared to many-body model, two-body model provides a concise way of thinking about and charactering interactions between atoms in an ensemble [5]. In addition, at sufficient low densities where the atom separation is much larger than extent of the Rydberg wavefunctions, the principal atom-atom interaction is of the DD form. Accordingly, in this region, two-body DD coupling dominates atom-atom interactions [9][10]. So in this dissertation, all of the calculations and simulations are based on the two-body model.

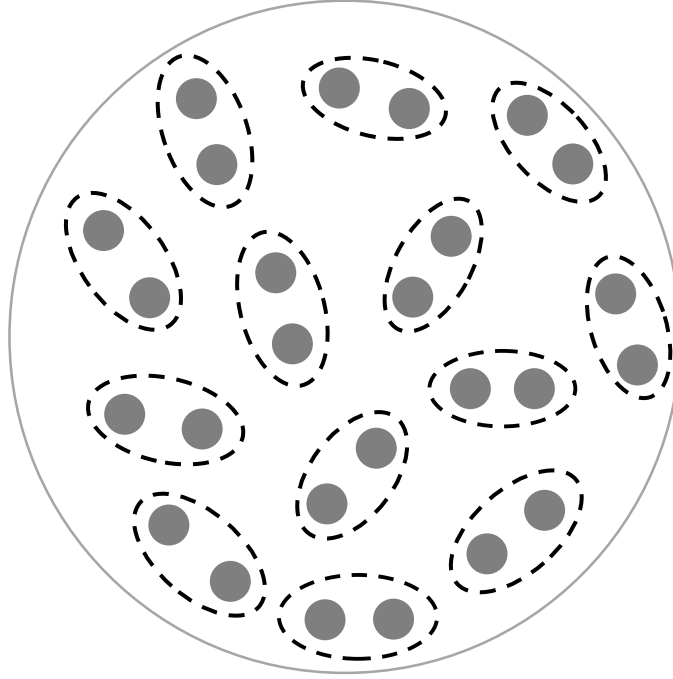


Figure 3.2: Schematic of atom pairs in a MOT. For each atom in the MOT, we only consider the effect of its nearest neighbor. One atom and its nearest neighbor is considered to be “a pair of atoms”.

For each a pair of atoms, we can write their electronic state, in non-interacting basis, as the product of their individual states. For example, for a pair of atoms in a  $ns$  state and  $np$  state, respectively, we can write the state of this pair as  $nsnp$ . We call this state a “pair state”. Such a convention is followed in all sections of this dissertation.

### 3.2.2 Nearest Neighbor Distribution

We need to know the distance between atoms to determine the DD coupling between them. We use the so called “nearest neighbor distribution” to express the probability that an atom and its nearest neighbor in a random ensemble have a particular separation. The

nearest neighbor distribution function  $H(r)$  for point particles in a D-dimensional system is [11][12]:

$$H(r) = \rho \frac{dv_D(r)}{dr} \exp [-\rho v_D(r)] \quad (3.6)$$

where  $\rho$  is the density of the atoms and  $v_D(r)$  is the volume of the D-dimensional sphere.

For a 3-D system, we get the distribution function:

$$H(r) = 4\pi\rho r^2 \exp \left[-\frac{4}{3}\pi\rho r^3\right]. \quad (3.7)$$

From Equation (3.7), we find that the most possible nearest neighbor distance between atoms in a random ensemble is:

$$R \simeq \sqrt[3]{\frac{1}{2\pi\rho}}. \quad (3.8)$$

For a MOT with density  $\rho \approx 10^9 \text{ cm}^{-3}$  and a temperature  $T \sim 100 \text{ } \mu\text{K}$ , the most possible distance between one Rb atom and its nearest neighbor is about  $5 \text{ } \mu\text{m}$  and the velocity of the atoms is on the order of  $10 \text{ cm/s}$ . In  $1 \text{ } \mu\text{s}$ , one atom can move about  $0.1 \text{ } \mu\text{m}$  which is much smaller than the distance between two atoms. So we consider the atoms as “frozen” or static atoms in the MOT for experiments involving DD integration times  $< 1 \text{ } \mu\text{s}$ .

### 3.2.3 Förster Resonance Energy Transfer

Förster Resonance Energy Transfer (FRET) is a mechanism describing energy transfer between two atoms or molecules. It happens when two neighboring atoms are dipole-dipole coupled to higher and lower states with equal energy spacing. This mechanism can be described very easily using the two-body picture. As shown in Figure 3.3, one atom acts as an energy donor and the other one, an acceptor. The atoms exchange energy as the donor is de-excited to a lower state and the acceptor excited to a higher state via the DD interaction.

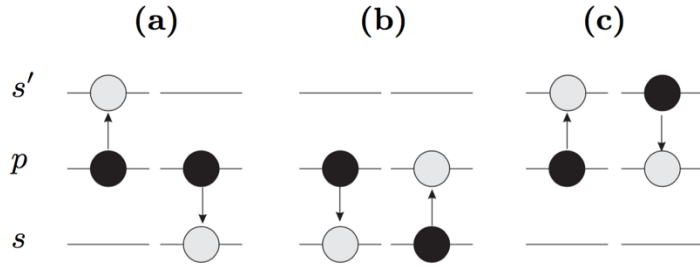


Figure 3.3: Schematic for typical FRET. Black cycles represent the initial pair states and gray cycles the final pair states. (a) is  $pp \rightarrow ss'$ , (b)  $ps \rightarrow sp$  and (c)  $ps' \rightarrow s'p$  [13].

### 3.3 Dipole-Dipole Interaction

In the above discussion, the DD interaction has been mentioned several times. For Rydberg atoms in the two-body approximation, it is straightforward to explicitly derive the form of the interaction.

#### 3.3.1 Dipole Moment

As noted previously, a Rydberg electron spends most of the time far from the positive core that binds it. Although the atom as a whole is neutral, classically it has a time dependent dipole moment:

$$\vec{\mu} = q\vec{r} \quad (3.9)$$

where  $q$  is the electron charge and  $\vec{r}$  is the vector from the negative charge to the positive charge. This classical physics perspective can help us understand the dipole-dipole interaction better.

In quantum physics, in the absence of external fields, an atom in an electronic eigenstate has no permanent dipole moment. However, field, or neighboring atoms can induce a dipole

moment. This dipole moment is known as a “transition dipole moment” as it is responsible for the transitions between state 1 and state 2, the linear combination of which can exhibit a permanent or time-dependent dipole moment:

$$\overrightarrow{\mu_{12}} = \langle 1 | \vec{r} | 2 \rangle \quad (3.10)$$

for  $q=e=1$ . From Equation (3.10) we see that if state 1 and state 2 are the same, then the transition dipole moment is 0, so the transition dipole moment appears as an off-diagonal matrix element in the system Hamiltonian.

The preceding discussion on atomic dipole moments has been divided into classical and quantum physics views. Similar to that, our DD interaction model will also be explored from both views.

### 3.3.2 Dipole-Dipole Interaction in the Classical Picture

The classic dipole-dipole interaction picture provides the basis for the interaction between quantum atoms, and helps us to understand the quantum picture.

If there is only one dipole, the potential of this dipole is merely provided by the attractive force between the positive charge and negative charge. When two dipoles in close proximity, the potential energy of such a system also induces the dipole-dipole interaction. Figure 3.4 illustrates the interaction between two dipoles. The total potential energy of this system does not only contain the inner coulomb potential of each individual dipole but also the potential caused by dipole-dipole interaction. The dipole-dipole interaction potential can be written as:

$$V_{dd} = \frac{q^2}{R} - \frac{q^2}{|\vec{r}_1 - \vec{R}|} - \frac{q^2}{|\vec{r}_2 + \vec{R}|} + \frac{q^2}{|\vec{r}_1 - \vec{r}_2 - \vec{R}|}. \quad (3.11)$$

From reference [14], assuming  $r_1, r_2 \ll R$ , Equation (3.11) can be simplified to:



$$V_{dd} = \frac{\vec{r}_1 \cdot \vec{r}_2 - 3(\vec{r}_1 \cdot \hat{R})(\vec{r}_2 \cdot \hat{R})}{R^3}, \quad (3.12)$$

where we assume  $q=e=1$ .

Expressed in terms of dipole moments, Equation (3.12) could also be written as:

$$V_{dd} = \frac{\vec{\mu}_1 \cdot \vec{\mu}_2 - 3(\vec{\mu}_1 \cdot \hat{R})(\vec{\mu}_2 \cdot \hat{R})}{R^3} \quad (3.13)$$

where  $\vec{\mu}_1$  is the dipole moment of atom 1 and  $\vec{\mu}_2$  is the dipole moment of atom 2. From this expression, we see that the interaction energy can be positive or negative depending on the relative orientation of the dipole moments and the line connecting them.

From Equation (3.13) we can also see the dipole-dipole interaction is strongly affected by the distance between the dipoles or Rydberg atoms. This is the reason why two-body effect is the major effect in an ensemble of frozen atoms.

Setting  $\hat{R} = \hat{z}$ , Equation (3.12) can be written as:

$$V_{dd} = \frac{x_1 x_2 + y_1 y_2 - 2z_1 z_2}{R^3} \quad (3.14)$$

where  $x_i$ ,  $y_i$ , and  $z_i$  specify the position of the Rydberg electron in the  $i$ th atom relative to the center of the atom.

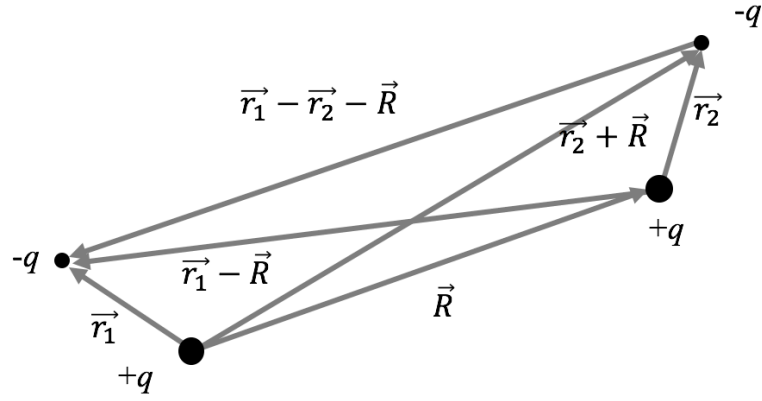


Figure 3.4: Schematic of the interaction between two classical dipoles.

### 3.3.3 Dipole-Dipole Interaction in the Quantum Picture

The quantum DD model derives from the classical picture. As an example, we consider a resonant interaction such as that shown in Figure 3.3a. Suppose an atom pair is initially in state  $pp$ , and we want to explore the evolution of the wavefunction in such a system. We define:

$$\psi_i = pp, \text{ and } \psi_f = ss'. \quad (3.15)$$

The total Hamiltonian of the system is  $H = H_0 + V$ , where  $V$  is the potential associated with the classical dipole-dipole interaction. The solution of the time-dependent Schrodinger equation,  $H\Psi = i\partial\Psi/\partial t$  yields the pair wavefunction which, in general, is a linear combination of  $\psi_i$  and  $\psi_f$ :

$$\Psi = C_i(t)\psi_i + C_f(t)\psi_f \quad (3.16)$$

where all of the time dependence is contained in the coefficients  $C_i(t)$  and  $C_f(t)$ . The Schrodinger equation can be written as:

$$\begin{pmatrix} C_i \\ C_f \end{pmatrix} \begin{pmatrix} E_i & V_{fi} \\ V_{if} & E_f \end{pmatrix} = i \begin{pmatrix} \dot{C}_i \\ \dot{C}_f \end{pmatrix} \quad (3.17)$$

where  $V_{pq} = \langle \psi_p | V | \psi_q \rangle$ , with  $p$  and  $q$  representing pair states. By solving Equation (3.17) we can get two eigen energy values:

$$\begin{cases} E_1 = \frac{(E_i + E_f) + \sqrt{(E_i + E_f)^2 - 4(E_i E_f - M^2)}}{2} \\ E_2 = \frac{(E_i + E_f) - \sqrt{(E_i + E_f)^2 - 4(E_i E_f - M^2)}}{2} \end{cases} \quad (3.18)$$

where  $M$  is expressed as:

$$M = |\langle pp | V | ss' \rangle| \propto \frac{|\langle p | r_1 | s \rangle| \cdot |\langle p | r_2 | s' \rangle|}{R^3} = \frac{|\mu_{ps} \mu_{ps'}|}{R^3}. \quad (3.19)$$

This expression utilizes the concept of transition dipole moment mentioned in section 3.3.1.

When in resonance,  $E_1 = E_2 = E$ , Equation (3.18) evolves to:

$$\begin{cases} E_1 = E + M \\ E_2 = E - M \end{cases} \quad (3.20)$$

We can also obtain two eigenstates from Equation (3.17) if  $E_1 = E_2 = E$ :

$$\begin{cases} \psi_1 = (\psi_i + \psi_f)/\sqrt{2} \\ \psi_2 = (\psi_i - \psi_f)/\sqrt{2} \end{cases} \quad (3.21)$$

So the complete solution of the Equation (3.17) is:

$$\Psi = C_1 \psi_1 e^{-iE_1 t} + C_2 \psi_2 e^{-iE_2 t} \quad (3.22)$$

in which  $C_1$  and  $C_2$  are constants determined by the initial condition.

The above discussion gives the approach for dealing with dipole-dipole interactions in a simple two-state system. To calculate the matrix elements for such a system and more complicated systems, we need to go deeper and consider the relative orientation of the

atomic dipole relative to the inter nuclear axis. By separating the radial part and the angular parts of the interaction matrix element, the calculation is implemented as follows.

From Equation (3.14), using the relations between the Cartesian coordinates and the spherical harmonics ( $Y_{lm}$ ),

$$\begin{aligned} x &= \sqrt{\frac{2\pi}{3}} r (-Y_{11} + Y_{1-1}) \\ y &= i \sqrt{\frac{2\pi}{3}} r (Y_{11} + Y_{1-1}) \\ z &= \sqrt{\frac{4\pi}{3}} r Y_{10} \end{aligned} \quad (3.23)$$

the dipole-dipole interaction can be written in terms of spherical harmonics as:

$$V_{dd} = -\frac{r_1 r_2}{R^3} \cdot \frac{4\pi}{3} \cdot ({}^1Y_{11} {}^2Y_{1-1} + {}^1Y_{1-1} {}^2Y_{11} + 2 {}^1Y_{10} {}^2Y_{10}) \quad (3.24)$$

where  ${}^iY_{lm}$  is the spherical harmonics acting on the Rydberg electron of the  $i$ th atom, and  $r_j$  is purely radial part of the transition matrix element in atom  $j$ .

To compute the matrix elements, Edmond's  $C$ -tensors are introduced [15]. The relation between the spherical harmonic tensors and the  $C$ -tensors is:

$$C_q^k = \sqrt{\frac{4\pi}{2k+1}} Y_{kq}. \quad (3.25)$$

So the dipole-dipole interaction in form of  $C$ -tensors is:

$$V_{dd} = -\frac{r_1 r_2}{R^3} (C_1^1 C_{-1}^1 + C_{-1}^1 C_1^1 + 2 C_0^1 C_0^1). \quad (3.26)$$

In Equation (3.26), a pair of  $C$ 's implies that the first  $C$  acts on the first atom and the second  $C$  on the second atoms.

Equation (3.26) is used in the simulation to calculate the matrix elements. As an example, the dipole-dipole matrix element between  $p_{\frac{1}{2}\frac{1}{2}}p_{\frac{1}{2}\frac{1}{2}}$  and  $s_{\frac{1}{2}\frac{1}{2}}s'_{\frac{1}{2}\frac{1}{2}}$  is expressed as:

$$\langle p_{\frac{1}{2}\frac{1}{2}}p_{\frac{1}{2}\frac{1}{2}} | V_{dd} | s_{\frac{1}{2}\frac{1}{2}}s'_{\frac{1}{2}\frac{1}{2}} \rangle = -\frac{r_1 r_2}{R^3} \langle p_{\frac{1}{2}\frac{1}{2}} | C_0^1 | s_{\frac{1}{2}\frac{1}{2}} \rangle \langle p_{\frac{1}{2}\frac{1}{2}} | C_0^1 | s'_{\frac{1}{2}\frac{1}{2}} \rangle \quad (3.27)$$

where state of each atom is expressed as  $\ell_j m_j$ . The radial matrix elements can be calculated using a numerical Numerov integration algorithm [18].

### 3.3.4 Dipole-Dipole Coupled System in an Electric Field

In some of the experiments, we utilize THz pulses to coherently redistribute population among Rydberg states. The THz pulse can be treated as a time-dependent electric field. To simulate the redistribution process, we need to model the DD system in the electric field.

The model is based on the picture shown in Figure 3.4. We define the vector pointing from one atom core to the other core as the  $z$ -axis. The electric field has an angle  $\theta$  relative to the  $z$  axis. We define the plane containing the electric field vector and the  $z$  axis as the  $xz$  plane.

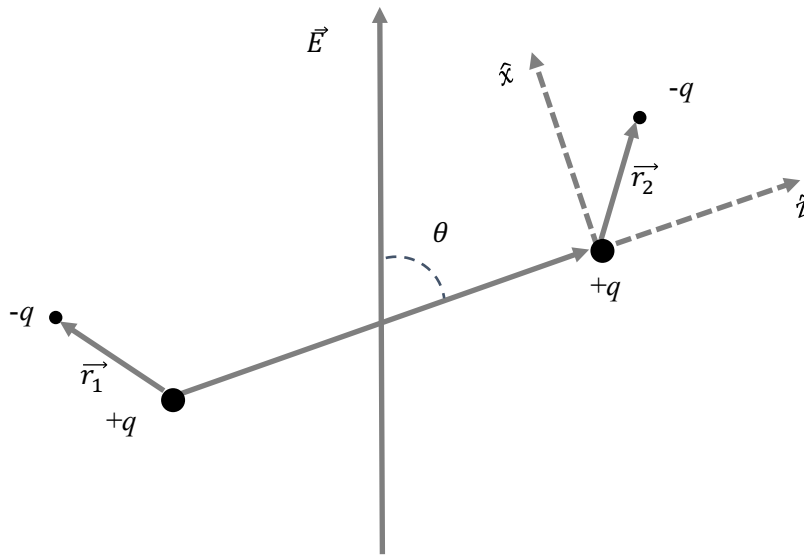


Figure 3.5: Schematic for a DD system in an electric field.

As shown in Figure 3.5, for the electron in atom 1, the effect of the electric field is:

$$H_1 = -q\vec{E} \cdot \vec{r}_1 = -qE_0(\sin\theta\vec{x}_1 + \cos\theta\vec{z}_1) \quad (3.28)$$

where  $E_0$  is the amplitude of the electric field, which is time-dependent for the THz pulse.

From Equation (3.23) and (3.25), the above equation can be re-expressed as:

$$H_1 = -q\vec{E} \cdot \vec{r}_1 = -qE_0r_1\left(\frac{\sin\theta}{\sqrt{2}}(C_1^1 + C_{-1}^1) + \cos\theta C_0^1\right). \quad (3.29)$$

For a randomly distributed ensemble composed of many pairs of atoms, each pair has its own defined  $z$  axis, thus  $\theta$  is different for different pairs.

A similar expression applies to atom 2. So the Hamiltonian associated with the applied electric field in a DD system is:

$$H_E = H_1 + H_2. \quad (3.30)$$

We already know the form of dipole-dipole interaction. Using perturbation theory, we can calculate the evolution of wavepackets in a random ensemble under the influence of dipole-dipole interaction, as well as the state redistribution when the THz pulses are applied to the atoms.

### 3.4 Blackbody Radiation Model

Rydberg atoms are strongly affected by blackbody radiation, even at room temperature. The strong influence of thermal radiation is due to two reasons [5]. First, the energy spacing between adjacent Rydberg levels is small ( $\Delta E \propto n^{-3}$ ), so that  $\Delta E$  can be  $< KT$  at 300K. Second, the dipole matrix elements for transition between adjacent Rydberg states are enormous, scaling as  $n^2$ , providing a large coupling between atoms at the thermal radiation. Because of this strong coupling, population initially in one state can rapidly diffuse to other energetically nearby states due to blackbody radiation.

### 3.4.1 Blackbody Induced Transition

The spontaneous decay rate of a state  $n\ell$  to a lower lying state  $n'\ell'$  is given by the Einstein  $A$  coefficient  $A_{n'\ell',n\ell}$  [16]. The thermal radiation induced stimulated emission rate is:

$$K_{n'\ell',n\ell} = \bar{n}A_{n'\ell',n\ell}, \quad (3.31)$$

where  $\bar{n}$  is the photon occupation number [17],

In terms of the average oscillator strength, Equation (3.31) can be reexpressed as:

$$K_{n'\ell',n\ell} = -2\bar{n}\alpha^3 w_{n'\ell',n\ell}^2 \bar{f}_{n'\ell',n\ell} \quad (3.32)$$

where  $\alpha$  is the fine structure constant,  $w_{n'\ell',n\ell}$  is the energy difference  $W_{n'\ell'} - W_{n\ell}$ ,

$$\bar{f}_{n'\ell',n\ell} = \frac{2}{3} w_{n'\ell',n\ell} \frac{\ell_{\max}}{2\ell+1} |\langle n'\ell' | r | n\ell \rangle|^2, \quad (3.33)$$

and  $\ell_{\max}$  is the larger of  $\ell$  and  $\ell'$ .

Equation (3.32) and Equation (3.33) are used in Chapter 4 to calculate the blackbody radiation induced transition rate between nearby Rydberg levels.

### 3.4.2 Radiation Model

When considering the decay of the population from a single Rydberg state, as described in Chapter 4, radiation models similar to the schematic in Figure 3.6 are used. There is spontaneous decay into lower lying states. There is blackbody induced transition between the starting state and its higher and lower energy neighbors. There is also blackbody radiation between one neighbor and the neighbor's neighbors, and so on.

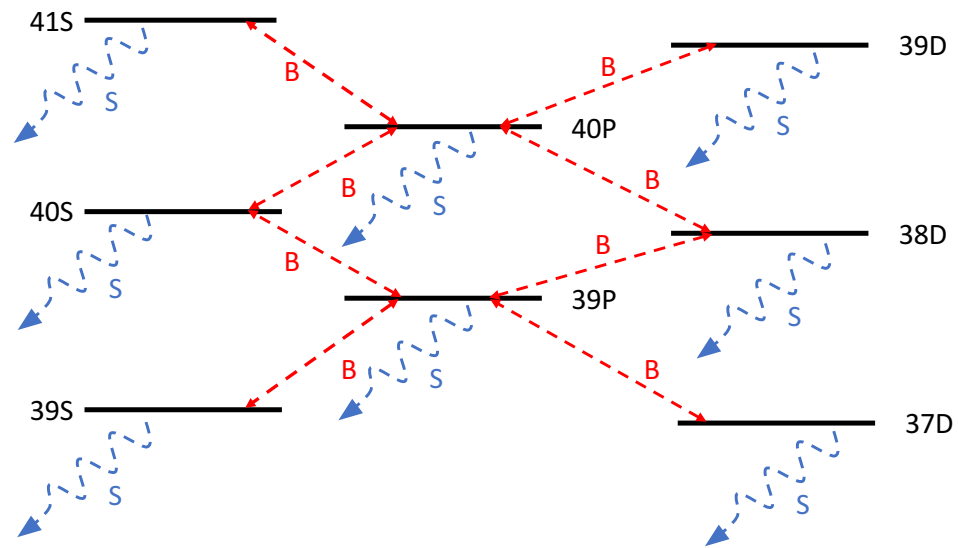


Figure 3.6: Decay model for atoms starting from state 40s as an example. The red dash lines between two states indicate blackbody stimulated transitions between these two states. The blue dash curves represent the spontaneous decay.

In reality, there are more states involved in the decay and transition process and the situation is much more complicated. But for calculation convenience, a limited number of nearby states are chosen. To make sure such a simplification is reasonable, results based on different numbers of states are compared to find an essential set of nearby states which agrees well with the calculation performed with additional states.



# Bibliography

- [1] H. E. White, *Introduction to Atomic Spectra*, McGraw-Hill, New York (1934).
- [2] G. D. Living and J. Dewa, *Proc, Roy, Soc. Lond*, 29, 398 (1879).
- [3] W. N. Hartley, *J. Chem. Soc.* 43, 390 (1883).
- [4] J. R. Rydberg, *Phil. Mag.* 5<sup>th</sup> Ser. 29, 331 (1890).
- [5] Thomas F. Gallagher. *Rydberg Atoms*. Cambridge University Press (1994).
- [6] R. Shankar, *Principles of Quantum Mechanics*, 2<sup>nd</sup> Edition, Plenum Press (1994).
- [7] M. J. Seaton, *Rep. Prog. Phys.* 46, 167 (1983).
- [8] Thomas F. Gallagher. *Rep. Prog. Phys.* 51, 143 (1988).
- [9] B. Sun and F. Robicheaux, *Spectral Linewidth Broadening from Pair Fluctuations in A Frozen Rydberg Gas*, *Phys. Rev. A.* 78, 040701 (2008).
- [10] I. Mourachko, D. Comparat, F. de Tomasi, A. Fioretti, P. Nosbaum, V. M. Akulin, and P. Pillet, *Many-Body Effects in a Frozen Rydberg Gas*, *Phys. Rev. Lett.* 80, 253 (1998).
- [11] S Torquato, B Lu and J Rubinstein, *Nearest-neighbour Distribution Function for Systems of Interacting Particles*, *J. Phys. A: Math. Gen.* 23 (1990)
- [12] Hertz P, *Math. Ann.* 67, 387 (1909).
- [13] S. Westermann, T. Amthor, A.L. de Oliveira, J. Deiglmayr, M. Reetz-Lamour, and M. Weidemuller, *Dynamics of resonant energy transfer in a cold Rydberg gas*, *Eur. Phys. J. D* 40, 37–43 (2006).
- [14] F. Robicheaux, J. V. Hernández, T. Topçu,<sup>1</sup> and L. D. Noordam, *Simulation of Coherent Interactions between Rydberg Atoms*, *Phys. Rev. A.* 70, 042703 (2004).
- [15] A. R. Edmonds, *Angular Momentum in Quantum Mechanics*, Princeton University Press, Princeton (1960).

- [16] H. A. Bethe and E. A. Salpeter, Quantum Mechanics of One-and-Two-Electron Atoms, Academic Press, New York (1957).
- [17] R. Loudon, The quantum Theory of Light, Oxford University Press, London (1973).
- [18] M. L. Zimmerman, M. G. Littman, M. M. Kash, and D. Kleppner, Rydberg States of Atoms and Molecules, Phys. Rev. A 20, 2251 (1979).

## 4 Absence of Collective Decay in a Cold Rydberg Gas

We have studied the decay of Rydberg excitations in a cold Rb gas. A 10 ns, pulsed-dye-amplified diode laser excites Rb atoms at 70  $\mu$ K in a magneto-optical trap to  $ns$  or  $np$  Rydberg states with principal quantum numbers  $26 \leq n \leq 40$ . Time-delayed state-selective field ionization is used to directly monitor the population in the initial and neighboring Rydberg levels. The measured time dependence of the Rydberg population is well described by numerical simulations which consider only spontaneous emission and population transfer by blackbody radiation. No evidence for collective decay is found at atom densities up to  $3 \times 10^9 \text{cm}^{-3}$ . This result is in contrast to a previous study [Wang *et al.*, Phys. Rev. A 75, 033802 (2007)], in which superradiant decay was theoretically predicted and experimentally inferred for atom density and laser focal volume conditions very similar to those considered here. Suppression of collective emission is likely due to variations in transition energies within the atom sample, dominated by inhomogeneities in dipole-dipole exchange interactions for initial  $s$  states, or by a combination of dipole-dipole and electric field inhomogeneities for the initial  $p$  states.

## 4.1 Introduction

Atoms within cold Rydberg ensembles are coupled by strong long-range dipole-dipole (DD) interactions [1], making them interesting systems for exploring few- and many-body quantum dynamics in general and applications in quantum information in particular [2–35] (The properties of Rydberg Atoms are described in Chapter 3). Of course, unlike in ground-state systems, finite Rydberg lifetimes limit the types of measurements and number of coherent manipulations that can be performed in a given experiment. Fortunately, isolated Rydberg atoms exhibit low spontaneous decay rates [1], potentially enabling processing over micro- to millisecond time scales. At first glance this stability against radiative decay might seem surprising given the large transition matrix elements between adjacent Rydberg states, which scale as  $n^2$ . However, spontaneous decay to nearby levels via low-frequency emission is strongly suppressed by the  $\omega^3$  dependence of the Einstein  $A$  coefficient. As a result, the predominant decay path for isolated Rydberg atoms in low-angular-momentum states is to the ground or low-lying excited levels, resulting in an  $n^{-3}$  scaling of the spontaneous emission rate.

That said, neighboring Rydberg levels can play a dominant role in the decay of a large number  $N$  of atoms which either are simultaneously excited in a volume with dimensions smaller than the wavelength  $\lambda$  of the emitted light, or are sequentially excited throughout a cylindrical volume with length  $L \gg \lambda$  [36,37]. In his seminal paper [38], Dicke predicted that a dense collection of  $N$  radiators, either in very close proximity or in a properly phased extended distribution, could develop spontaneous correlations and collectively emit radiation at rates greatly exceeding (“superradiance”), or much smaller than (“subradiance”), those of individuals in the sample. For the two-level systems considered by Dicke, correlations between a large number of emitting atoms can initiate collective superradiant emission at a per atom rate up to  $N/4$  times larger than that between the same

two levels in an isolated atom [38]. Collective emission remains a subject of considerable interest in many different contexts, including Rydberg atoms [39–51].

The presence of blackbody radiation, the existence of multiple photo decay channels in a Rydberg ladder, and strong DD interactions between atoms, all explicitly neglected in Dicke’s original paper (and in many subsequent treatments) [38,52,53], make it much more difficult to observe, characterize, and quantitatively predict collective decay phenomena in Rydberg gases. In particular, DD interactions can suppress superradiance. In a thermal gas, this suppression results from DD-mediated collisions that homogeneously dephase the individual emitters in the ensemble at a rate greater than the superradiance rate [50]. In a frozen gas, DD exchange interactions couple pairs, or larger groups, of atoms leading to a variation in transition energies across the ensemble. Such inhomogeneities squelch the correlations that underlie superradiance, along with the collective emission [47]. That said, a clear signature of superradiance between Rydberg states, a fluorescence cascade from a Rydberg ladder proceeding at a rate much greater than spontaneous emission of isolated atoms, was first observed following pulsed-laser excitation of an elongated volume ( $L \gg \lambda$ ) in a thermal cell [36]. More recently, direct evidence for superradiance was found in the millimeter-wave emission from a large cylindrical volume of Ca Rydberg atoms in a supersonic expansion, also with  $L \gg \lambda$  [49,50]. As pointed out in the latter work, the rates for superradiant decay and DD dephasing within a given decay channel are essentially identical, up to a multiplicative geometric factor  $L/\lambda$  in the superradiance rate formula. Accordingly, it was suggested that collective decay should not play a major role in Rydberg depopulation unless  $L \gg \lambda$  [50].

Still, despite competing DD effects, under certain conditions superradiance should play some role in cold ensembles where the dimensions of the excited volume are less than or comparable to  $\lambda$ . Indeed, evidence of reduced Rydberg lifetimes has been reported in several such experiments [39,48,51,54,55]. For example, Feng et al. observed a density-

dependent lifetime suppression of Cs Rydberg atoms in a magneto-optical trap (MOT) [54]. They attribute the suppression to a combination of neutral Rydberg atom collisions and superradiance. However, the evidence for superradiance appears tenuous as their calculations with and without superradiant contributions both fall within their measurement uncertainty (see their Fig. 2). In addition, if one applies their values for Rydberg collision velocity and cross section, the collisional depopulation rates are over three orders of magnitude too small to account for their observations. Han and Maeda attributed population transfer from initial to neighboring Rb Rydberg states to superradiance, but provided no evidence ruling out other possible population transfer mechanisms [56]. In other measurements, using fluorescence detection, Day et al. found Rydberg depopulation rates that were roughly twice that expected from single-atom spontaneous emission over a range of  $n$  states and at low densities,  $\rho \sim 1 \times 10^7 \text{ cm}^{-3}$  [48]. The small variation of the lifetime suppression with principal quantum number coupled with trap loss measurements argued against collisional depopulation and blackbody ionization. Instead, the enhanced Rydberg decay rate was found to be qualitatively consistent with a simplified collective decay model. In other experiments, the inclusion of superradiant decay channels was found to improve the quality of model fits to electromagnetically induced transparency measurements in cold Rydberg gases [51,55].

Certainly, a substantial decrease in Rydberg lifetimes due to collective emission would have a significant impact on most cold Rydberg atom experiments. Perhaps more important, in the context of the exploration and control of few- or many-body Rydberg dynamics, are the influences of the spontaneous quantum correlations that are predicted to develop with the emission of the first photon from the sample and evolve as the Rydberg population descends through a ladder of Dicke states [38,53]. Interestingly, Wang et al. presented a sophisticated theoretical treatment of photo decay in a multilevel Rydberg system which makes definite predictions as to whether superradiance should occur for a given initial

principal quantum number, atom density, and experimental volume [39]. The theory apparently reproduced the rapid decay, at a rate approximately 40 times greater than predicted from spontaneous emission alone, of an initial population of  $43p$  atoms in a MOT at a density of  $\rho \sim 5 \times 10^8 \text{ cm}^{-3}$ .

We have used pulsed-laser excitation of Rb Rydberg atoms in a MOT under conditions ostensibly similar to those used in Ref. [39] in an attempt to test the predictions of their Rydberg superradiance theory. We employ state-selective field ionization (SSFI) to measure the population in the initial and neighboring Rydberg states as a function of delay after the laser excitation. We find no evidence for the predicted collective decay over a range of principal quantum numbers  $26 \leq n \leq 40$ , and atom densities  $\rho \sim 3 \times 10^9 \text{ cm}^{-3}$ , despite the fact that, for these states, our highest density is more than two orders of magnitude above the predicted superradiance threshold [39]. Instead, our measurements are consistent with noncorrelated spontaneous decay combined with population redistribution via blackbody radiation.

## 4.2 Experimental Procedure and Results

General information about the setup could be found in Chapter 2. This section provides some particular information about the experiment approach.

In the experiments,  $^{85}\text{Rb}$  atoms at  $70 \text{ } \mu\text{K}$  are held in a MOT. The full width at half maximum (FWHM) diameter of the atom cloud is  $0.4 \text{ mm}$ . The MOT is positioned at the center of four parallel rods which facilitate the application of static and pulsed electric fields in the  $y$  direction for exciting and detecting Rydberg atoms in the MOT. A  $10 \text{ ns}$  pulsed, tunable, dye-amplified,  $\sim 480 \text{ nm}$  diode laser propagating in the  $x$  direction is focused into the center of the MOT, creating a cylindrically shaped volume of cold Rydberg atoms with a FWHM diameter of  $\sim 0.1 \text{ mm}$  and a length of  $0.4 \text{ mm}$ . The MOT and Rydberg lasers are

non collinear, preventing the excitation of Rydberg atoms throughout any extended volume from the lower-density background of thermal Rb atoms in the chamber. The  $\sim 100$  MHz bandwidth of the Rydberg excitation laser ensures that there is no excitation suppression via dipole blockade [2,3]. At a variable time  $\tau$  after the laser excitation, a ramped voltage is applied to two of the rods, ionizing any Rydberg atoms in the interaction region and pushing the resulting ions toward a micro channel plate (MCP) detector. Ions originating from different Rydberg states arrive at the detector at different times. The integrated signals in different time bins are proportional to the populations in different Rydberg states and are recorded for each laser shot as a function of the ionization time  $\tau$ . The experiment proceeds at the 15 Hz dye-laser repetition rate.

The diode laser is tuned to selectively excite atoms from the upper  $5p$  trap level to  $ns$  and  $np$  Rydberg states with  $26 \leq n \leq 40$ . Excitation of  $np$  states is facilitated by the application of a weak static electric field (from 30 V/cm at  $n=26$ , 16 V/cm at  $n=32$ , to 7 V/cm at  $n=40$ ). By saturating the Rydberg excitation using high laser fluence, we ensure that 50% of the  $5p$  atoms within the interaction volume are excited to Rydberg states, enabling us to determine the Rydberg atom density [57]. Subsidiary experiments on resonant energy transfer between Rydberg atoms are consistent with the Rydberg density determination [57,58]. The MOT fluorescence is monitored throughout the lifetime measurements, ensuring that the number of atoms in the MOT is constant to within a few percent as  $\tau$  is scanned. Care is taken to minimize the amplified spontaneous emission from the dye-amplified laser pulse, eliminating direct photoionization of  $5p$  atoms. For the  $s$ -state measurements, a small,  $\sim 1.5$  V/cm, residual electric field persists in the interaction region due to imperfect shielding of the high voltage biased MCP (a larger field is present for initial  $p$  states). This field is sufficient to eject any ions or electrons from the interaction region, eliminating extended interactions between charged particles and neutral Rydberg atoms, and preventing the spontaneous evolution of the Rydberg gas into a plasma [59,60].



Neither the small static field employed for the  $p$ -state measurements nor the smaller residual field present during the  $s$ -state measurements substantially alters the rates for spontaneous emission or population transfer induced by blackbody radiation. The potential influence of the field inhomogeneity on superradiant decay is considered in the Analysis and Discussion section below.

Figure 4.1 and Figure 4.2 show our principal experimental results. In Figure 4.1 (a) and (c), the probabilities for finding atoms in the  $26s + 25p$ ,  $32s$ , and  $40s$  states are plotted as functions of detection time  $\tau$  for the maximum densities explored,  $\rho \sim 3 \times 10^9 \text{ cm}^{-3}$  and  $\rho \sim 1.5 \times 10^9 \text{ cm}^{-3}$ , respectively. Note that for the lowest initial  $n$  state the sum of the  $26s$  and  $25p$  populations is shown since their corresponding features could not be adequately separated in the time-resolved field-ionization signal. Within experimental uncertainties, the decays for the three initial  $s$  states are identical at the two densities shown. Additional measurements were made at Rydberg densities as low as  $\rho \sim 2 \times 10^8 \text{ cm}^{-3}$  (for  $32s$  initial states) and  $\rho \sim 5 \times 10^8 \text{ cm}^{-3}$  (for  $32p$  initial states), but no statistically significant differences were observed in the decays.

For spontaneous decay of isolated atoms at absolute zero, one would expect lifetimes of 28 and 58  $\mu\text{s}$  for the  $32s$  and  $40s$  atoms, respectively [61]. The measured lifetimes for the  $32s$  and  $40s$  states are substantially smaller, 19 and 38  $\mu\text{s}$ , respectively, due to population redistribution by blackbody radiation from the 300 K environment surrounding the MOT. Indeed, redistributed population is detected in neighboring Rydberg levels. In particular, Figure 4.1 (b) and (d) show the delay-dependent population in the  $p$  states ( $26p$ ,  $32p$ , and  $40p$ ) that lie immediately above the respective initial  $s$  states. Although we would expect to find some atoms in the adjacent, lower-lying  $p$  states as well, small features reflecting that population in the time-of-ionization signal lie within the initial-state peak (for the case of  $26s$ ) or are masked by the tail of the larger, initial-state peak which precedes it.

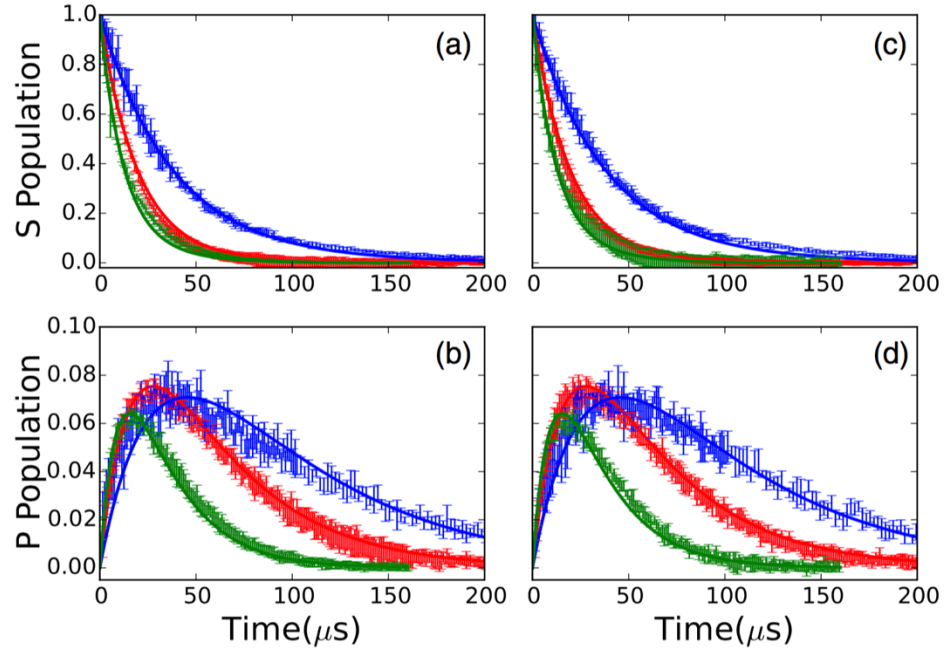


Figure 4.1: (a), (c) Probabilities for finding atoms in  $26s + 25p$  (green, fastest decay),  $32s$  (red, intermediate decay), and  $40s$  (blue, slowest decay) as a function of detection time  $\tau$  for Rydberg densities of  $\rho \sim 3 \times 10^9 \text{ cm}^{-3}$  (a) and  $\rho \sim 1.5 \times 10^8 \text{ cm}^{-3}$  (c). Note that the sum of the  $26s$  and  $25p$  populations is shown since their corresponding features could not be adequately separated in the field-ionization signal. Vertical bars show the experimental data with uncertainties, and the solid curves are calculated as described in the text. Measurements and calculations for the  $40s$  decay extend to  $500 \mu\text{s}$  where the remaining population is negligible. (b), (d) Probabilities for finding atoms in  $26p$  (green, fastest rise and decay),  $32p$  (red, intermediate rise and decay), and  $40p$  (blue, slowest rise and decay) levels as a function of detection time  $\tau$ . The states are populated by blackbody redistribution from the initial  $26s$ ,  $32s$ , and  $40s$  levels, respectively. The data were measured simultaneously with those shown in (a) and (c). Vertical bars show the experimental data with uncertainties, and the solid curves are calculated as described in the text. The measured  $p$ -state probabilities are normalized to the calculations as described in the text. The calculations have no free parameters and consider only the effects of spontaneous emission and blackbody radiation on isolated atoms.

The measured lifetime for the combined  $26s + 25p$  states is  $14 \mu s$ , the same as that expected from spontaneous decay of the  $26s$  level alone [61]. Simulations (described in detail below) indicate that this apparent agreement is not due to the absence of blackbody transfer out of  $26s$ . Rather, the small longer-lived  $25p$  component of the signal masks much of the change in the  $26s$  decay, with a predicted effective lifetime of  $13 \mu s$  for the  $26s + 25p$  combination, similar to what we observe. We note that due to the slow rate of the ionizing field, there is a distribution of ionization times and, therefore, of detection efficiencies for atoms in different states. As a result, each of the measured  $p$ -state populations in Figure 4.1 (b) and (d) has been multiplied by a normalization factor to obtain the best agreement with the calculated decay curves that are shown in the figures and described in the next section.

Figure 4.2 shows analogous data for the decay of initially excited  $26p$ ,  $32p$ , and  $40p$  states. Again, due to blackbody redistribution, the lifetimes associated with these decays ( $18$ ,  $31$ , and  $51 \mu s$ ), are considerably smaller than expected from spontaneous emission alone ( $37$ ,  $75$ , and  $155 \mu s$ ) [61]. However, in this case, no substantial population is detected in the neighboring  $s$  or  $d$  levels. The analysis described in the next section indicates that the populations in these states are not detectable within our signal-to-noise ratio, remaining at or below the few percent level due to the relatively rapid spontaneous emission rate out of the  $s$  states, and smaller  $p \rightarrow s$  and  $p \rightarrow d$  blackbody transition rates.

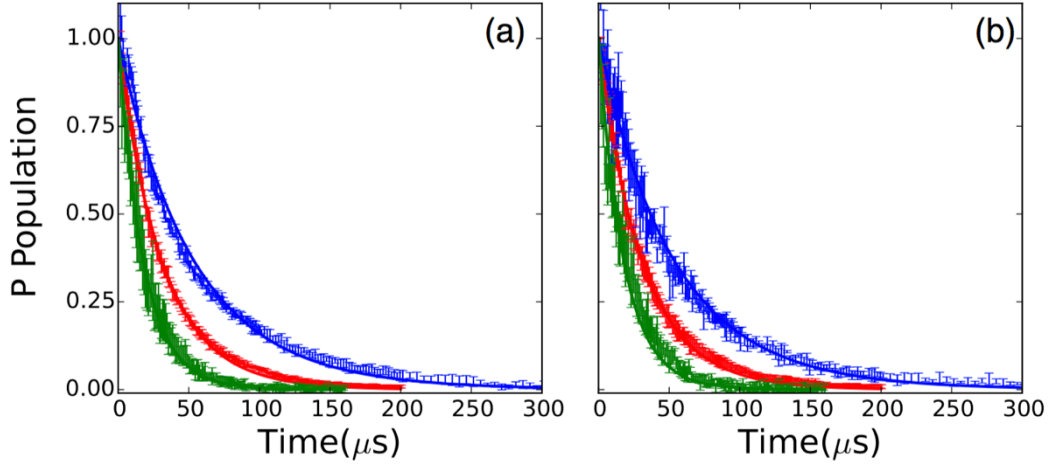


Figure 4.2: Probabilities for finding atoms in  $26p$  (green, fastest decay),  $32p$  (red, intermediate decay), and  $40p$  (blue, slowest decay) as functions of detection time  $\tau$  for Rydberg densities of  $\rho \sim 3 \times 10^9 \text{ cm}^{-3}$  (a) and  $\rho \sim 1.5 \times 10^9 \text{ cm}^{-3}$  (b). Vertical bars show the experimental data with uncertainties, and the solid curves are calculated as described in the text. Measurements and calculations for the  $40p$  decay extend to  $500 \mu\text{s}$  where the remaining population is negligible. The calculations have no free parameters and consider only the effects of spontaneous emission and blackbody radiation on isolated atoms.

### 4.3 Analysis and Discussion

To determine if collective processes play any significant role in the decays we observe, we compare the measurements to the results of a simple rate equation model which has an example schematic shown in Figure 3.6. The model includes population transfer via stimulated emission and absorption of blackbody radiation between an essential set of  $s$ ,  $p$ , and  $d$  Rydberg states neighboring the initial level, as well as spontaneous emission out of those essential states to (undetected) lower-lying levels. We calculate the blackbody transition rates between the essential states [1] as well as the known total spontaneous emission rates of the  $s$ ,  $p$ , and  $d$  Rydberg levels.

For example, for an initially excited  $40s$  state, the rate equation describing the time-dependent population in the initial  $40s$  level is:

$$\frac{dN_{40s}}{dt} = (-A_{40s} - B_{40s \rightarrow 40p} - B_{40s \rightarrow 39p})N_{40s} + B_{39p \rightarrow 40s}N_{39p} + B_{40p \rightarrow 40s}N_{40p} \quad (4.1)$$

where  $N_{n\ell}$  is the population in state  $n\ell$ ,  $A_{40s}$  is the  $40s$  spontaneous decay rate, and  $B_{n\ell \rightarrow n'\ell'}$  is the blackbody transition rate from  $n\ell$  to  $n'\ell'$ :

$$B_{n'\ell',n\ell} = -2\bar{n}\alpha^3 w_{n'\ell',n\ell}^2 \bar{f}_{n'\ell',n\ell} \quad (4.2)$$

which is mentioned in Chapter 3.

The populations in the secondary states  $39p$  and  $40p$  are computed using similar rate equations that include the total spontaneous decay rate out of those levels as well as blackbody transitions to and from pairs of  $s$  and  $d$  levels that lie immediately above and below each  $p$  state. We truncate the system of equations with rate equations that include spontaneous decay from the tertiary  $s$  and  $d$  levels and their blackbody couplings with the secondary states. Analogous systems of equations are used to compute the Rydberg population decay following initial  $p$ -state excitation. We note that, for initial or intermediate  $p$  states in particular, blackbody radiation redistributes a small, but non-negligible, fraction of the initial population beyond the nearest-neighbor  $s$  and  $d$  states. Therefore, an approximate expression

$$B_{n\ell} = \frac{4\alpha^3 kT}{3n^2} \quad (4.3)$$

for the total blackbody decay rate from each  $p$  level is used to more accurately account for the net transfer out of these states.

The results of our calculation, which ignore any collective decay phenomena, are shown with the data in Figure 4.1. Overall, the agreement is reasonable. Aside from the previously noted renormalization of the experimental  $p$ -state population, no parameter

adjustments have been made to obtain the level of agreement shown. The data provides no evidence of a significant reduction in the Rydberg lifetimes due to superradiance. This is true over a range of principal quantum numbers and atom densities where superradiant emission has been predicted to be the dominant decay path [39].

It is well established that superradiance is suppressed by inhomogeneities in transition energies across a sample of emitters [47], and we suspect that this is the case in our, and many other, cold atom experiments. In our experiments, three different effects contribute to such inhomogeneities. The first, and dominant mechanism for some of our measurements, is the DD exchange interaction. Consider a pair of identical atoms with two levels  $s$  and  $p$  and interatomic separation  $R$ . Spontaneous emission from the initial upper pair state  $ss$  results in the population of the bright configuration of the lower-energy pair state  $(sp + ps)/\sqrt{2}$ . However, due to the DD coupling between the atoms,  $V_{DD} \propto |\langle s|r|p \rangle|^2/R^3$ , the energy of this state is not the same as that for two atoms at infinite separation [1]. Accordingly, in a large ensemble of randomly spaced atoms, every possible configuration of  $N_s$   $s$  atoms and  $N_p$   $p$  atoms has a different energy, depending on the separation (and relative orientation) between the  $p$  atoms and their neighboring  $s$  atoms. As a result, any Dicke state, the bright linear combination of all possible configurations of  $N_s$   $s$  atoms and  $N_p$   $p$  atoms [38], is nonstationary. The phases of the constituent  $N$ -atom product states evolve at different rates, as determined by their DD energy shifts relative to their energies at infinite separation. The emission from these nonstationary Dicke states dephases at a rate comparable to the typical dipole-dipole energy shift  $V_{DD}$  for pairs of atoms in the ensemble. Superradiance cannot occur unless the system transitions down each step in the Dicke ladder more rapidly than this dephasing. A similar argument has been made by Gross and Haroche [62]. In the frequency domain, atoms with different transition energies at different locations in the ensemble do not collectively emit into the same field unless that emission occurs in a very short burst with a sufficiently broad, coherent bandwidth.

To determine the DD dephasing rate, we use the most probable nearest-neighbor separation in a random ensemble as we mentioned in 3.2.2,  $R \simeq (2\pi\rho)^{-3}$ , and average over all orientations of the Rydberg states on any two neighboring atoms  $ns$  and  $n'p$  to obtain [63,64]:

$$\overline{V_{DD}} = \frac{8\pi}{9} \rho |\langle ns|r|n'p \rangle|^2 \quad (4.4)$$

Using a numerical Numerov integration algorithm to compute the relevant radial matrix elements [65], at the highest density studied ( $\rho = 3 \times 10^9 \text{ cm}^{-3}$ ) we obtain values for the DD exchange coupling between the  $ns$  and  $(n-1)p$  states,  $\overline{V_{DD}} = 2.4, 6.2$ , and  $17 \text{ MHz}$ , for  $n = 26, 32$ , and  $40$ , respectively. These interaction strengths set effective lower limits for the rates at which collective emission from  $ns$  to  $(n-1)p$  can occur. Similarly, for initial  $np$  states and  $\rho = 3 \times 10^9 \text{ cm}^{-3}$ , the relevant exchange coupling is to the nearest lower-lying  $s$  states, with  $\overline{V_{DD}} = 3.1, 7.8$ , and  $20 \text{ MHz}$ , for  $n = 26, 32$ , and  $40$ , respectively.

The magnetic field gradient in the MOT is another source of energy inhomogeneities in our ensemble. As in Ref. [39], the magnetic field remains on during our measurements, resulting in a transition energy variation of approximately  $1 \text{ MHz}$  across the MOT. This inhomogeneity is smaller, or much smaller, than that due to dipole-dipole interactions at sufficiently high densities. It should not play a principal role in suppressing superradiance under the conditions used to produce Figure 4.1 and Figure 4.2.

The third contributor to the Rydberg energy variations across the ensemble is electric field inhomogeneity. While the voltages applied to the field rods produce a field that is quite uniform over the MOT (predicted field variations of  $0.07\%$ , corresponding to  $21 \text{ mV/cm}$  for the largest applied field of  $30 \text{ V/cm}$  for the  $26p$  measurements) the residual field from the MCP is not as uniform. Using a combination of spectroscopic measurements and accurate Stark energy calculations, we determine an upper limit for the Rydberg energy inhomogeneity due to the nonuniformity of the electric field  $F$  in the interaction region.

First, we measure the transition frequencies for excitation of  $32p_{3/2} |m_j| = 1/2, 3/2$ , from the  $5p_{3/2}$  upper trap state as a function of the voltage applied to the field rods (see Figure 4.3). For convenience, in the following discussion we refer to the field produced by the rods as the “applied” field. The experimental geometry is identical to that used for the lifetime measurements, but the Rydberg excitation is performed with an unamplified,  $3 \mu\text{s}$  pulse chopped from the  $\sim 1$  MHz bandwidth cw diode laser. The Rydberg excitation pulse has  $\sim 1 \mu\text{s}$  rise and fall times and is formed using an acousto-optic modulator. We use a temperature- and pressure-stabilized Fabry-Pérot interferometer to track the relative frequency of the Rydberg laser as it is scanned. The population in  $|m_j| = 1/2$  is distinguished from that in  $|m_j| = 3/2$  using SSFI. By recording the signal in two different time bins we obtain (nominally) separate excitation profiles to the two  $|m_j|$  states in the same laser frequency scan. Therefore, the energy splitting between the two  $m_j$  states can be accurately determined to well within the excitation bandwidth which is dominated by the 6.07 MHz natural linewidth of the initial  $5p_{3/2}$  level.

In zero electric field, the excitation profiles associated with the population in the two  $|m_j|$  levels should exhibit maxima at the same laser frequency, i.e., have zero energy splitting. However, as shown in Figure 4.4, we observe a minimum splitting of 2 MHz at an applied field of  $-2.8$  V/cm. The minimum splitting at nonzero applied field allows us to determine the components of the MCP field parallel and perpendicular to applied field. Apparently, the application of a  $-2.8$  V/cm rod field minimizes the net field in the interaction region. Accordingly, there must be a parallel, 2.8 V/cm, MCP field component which we call the “offset” field. Using the variation in the  $|m_j|$  splitting as a function of applied field, we can also extract a value, 1.5 V/cm, for the perpendicular, i.e., “residual,” MCP field component. The solid curve shown with the data in Figure 4.4 is the predicted  $32p_{3/2} |m_j| = 1/2, 3/2$  splitting as a function of applied field (extracted from a full numerical



Stark map calculation based on the method of Zimmerman et al. [65]), assuming MCP offset and residual fields of 2.8 and 1.5 V/cm, respectively. The good agreement with experiment confirms the accuracy of the calculation as well as the offset and residual field determinations.

At, and near, the minimum splitting (i.e., in the presence of the residual field alone where the  $s$ -state decay measurements are performed), the  $|m_j|$  excitation resonances have minimum linewidths of 8 MHz (see Figure 4.3). As noted above, the predominant contribution to this linewidth is the 6.07 MHz natural width of the  $5p_{3/2}$  level. However, the laser bandwidth, Zeeman shifts due to magnetic field inhomogeneities, and Stark shifts due to inhomogeneities in the 1.5 V/cm residual field also contribute. Assuming that the laser spectrum and field distributions are Gaussian, we deconvolute the primary line shape as a Voigt profile, and extract a bandwidth of 3.9 MHz for the total Gaussian contribution. Accordingly, we obtain an upper-limit estimate for the electric field inhomogeneity by assuming it is the sole contributor to this width. From the Stark shift of the  $32p_{3/2} m_j = 1/2$  level,  $E = 6.5 \text{ MHz}/(\text{V/cm})^2 F^2$ , we determine that the maximum possible variation of the residual field across the interaction region is  $F_{res} = 0.20 \text{ V/cm}$ . Using this field inhomogeneity with the field-dependent Stark shifts of the respective levels, we can compute the maximum range of transition energies between the initial  $s$  states and the  $p$  states immediately below them (to which the dipole coupling is the strongest). For the  $26s \rightarrow 25p$ ,  $32s \rightarrow 31p$ , and  $40s \rightarrow 39p$  transitions, the maximum energy variations across the excitation region (with only the residual field present) are 0.43, 2.2, and 12 MHz, respectively. The transition energy variations are smaller for transitions to lower lying  $p$  states due to the  $n^7$  scaling of the Rydberg polarizability. So, at the highest densities we have explored, the energy inhomogeneities associated with the residual electric field are less, or much less, than those associated with the dipole-dipole exchange interaction.

Therefore, the electric field inhomogeneities do not hold the primary responsibility for the suppression of superradiance from any of the initial  $s$  states.

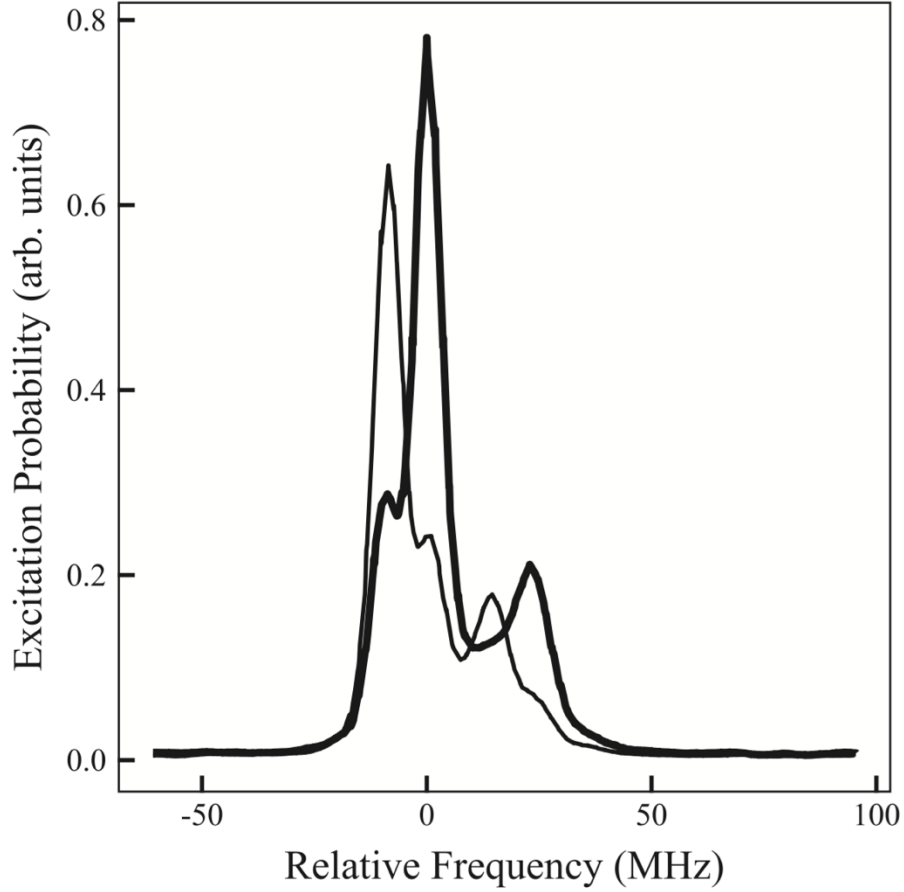


Figure 4.3: Measured  $32p_{3/2}$   $|m_j| = 1/2$  (bold line) and  $|m_j| = 3/2$  (thin line) excitation probabilities as a function of Rydberg laser frequency in zero applied field. The two data curves are obtained simultaneously in the same laser frequency scan. The small feature on the left (right) of the main  $|m_j| = 1/2$  ( $3/2$ ) peak is the result of imperfect discrimination of the  $|m_j| = 1/2$  and  $3/2$  components via SSFI. The additional peak on the right of the main feature in each trace is due to the trap-laser dressing of the  $5p_{3/2}$  and  $5s$  levels. Its frequency shift from the main peak reflects the Autler-Townes splitting of the  $5p_{3/2}$  initial state.

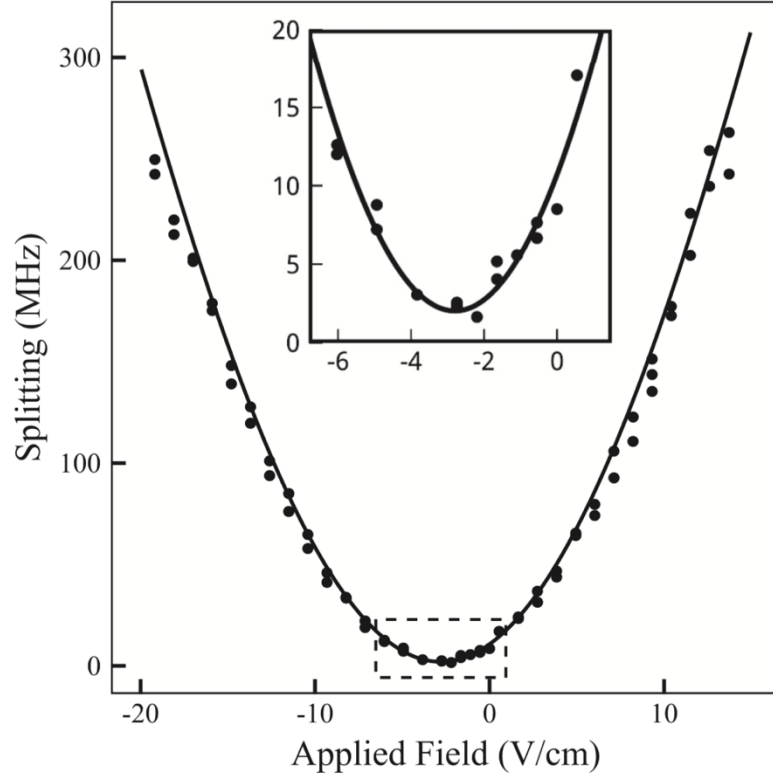


Figure 4.4: Difference (i.e., splitting) in the transition energies for exciting  $32p_{3/2} |m_j| = 1/2, 3/2$  from  $5p_{3/2}$  as a function of applied electric field. Filled circles are measurements and the solid curve is the result of a numerical Stark map calculation assuming orthogonal “offset” and “residual” electric field components due to the MCP of 2.8 and 1.5 V/cm, respectively. The inset shows a magnified view of the portion of the main figure within the dashed window.

The situation with the initial  $p$  states is somewhat different, as they are excited in a nonzero applied field that is considerably larger than the orthogonal residual field. As a result, the residual field and its inhomogeneity have essentially no effect on the transition energies. However, the spatial variations in the MCP offset field, which is parallel to the applied field, cannot be neglected. We use measurements of DD-mediated resonant energy transfer between Rydberg atoms to obtain an upper-limit estimate for the offset field

inhomogeneity. Those experiments use the same experimental geometry as the Rydberg decay measurements [58,64]. In the experiments, the probability for resonant population transfer from one pair of Rydberg states to another (e.g.,  $25s + 33s \rightarrow 24p + 34p$  [64]) is recorded as a function of an applied field which Stark-tunes the total energies of the atom pair in the two different configurations. In a uniform field, the line shape describing the field-dependent energy transfer probability is characterized by a peak at the “resonance” condition, where the total energies of the two sets of atom pair states are identical, and a width that is proportional to the Rydberg density. In a nonuniform field, the line shape has a nonzero minimum width as the density approaches zero, due to variations in the local field at different locations within the sample. Consider the  $25s + 33s \rightarrow 24p + 34p$  resonance [64] for which maximum population transfer occurs in an electric field of  $F \sim 3.4$  V/cm. Assuming that the nonzero resonance width that is observed at very low Rydberg density [64] is due solely to the inhomogeneity in the electric field (i.e., ignoring magnetic field inhomogeneities and any other broadening effects) we obtain the maximum possible variation in the offset field,  $F_{off} = 0.08$  V/cm, across the Rydberg sample. As an additional check, we consider a different energy transfer resonance,  $32p + 32p \rightarrow 33s + 32s$ , that is centered at a substantially higher field  $F \sim 11.5$  V/cm [58]. The nonzero low-density width for this energy transfer resonance gives the same maximum value for the offset field inhomogeneity,  $F_{off} = 0.08$  V/cm.

Given  $F_{off}$ , we can compute the maximum possible variations in the energies, associated with transitions between initial  $p$  states and the nearest lower-lying  $s$  state, due to the inhomogeneous field. Using  $F_{off}$ , the calculated Stark shifts of each of the states involved in the transitions  $26p \rightarrow 26s$ ,  $32p \rightarrow 32s$ , and  $40p \rightarrow 40s$ , and the applied fields employed for the respective  $p$ -state excitations, we obtain the maximum possible transition energy variations due to the inhomogeneous electric field. These are 4.9, 13, and 30 MHz

for the  $26p$ ,  $32p$ , and  $40p$  initial states, respectively. Accordingly, for the  $p$ -state decays, the maximum energy variations due to the field are comparable to, but up to a factor of  $1.7\times$  larger than, those due to dipole-dipole interactions. Given our likely overestimate of the field inhomogeneity, both may play a role in suppressing collective emission from the ensemble.

## 4.4 Conclusion

We have studied the decay of Rydberg excitations in a cold Rb gas and find no evidence for the dramatic decrease in lifetimes predicted by Wang et al. [39]. The decay rates and population redistribution we observe are consistent with a model that considers only spontaneous emission from, and blackbody redistribution within, isolated atoms. In our experiments, a small electric field in the interaction region ejects any free electrons or ions from the excitation volume, preventing ionization or population transfer due to interactions with charged particles. In addition, the lack of spatial overlap between the trapping lasers and the Rydberg excitation laser well outside of the cold atom cloud ensures that there is no Rydberg excitation within an extended volume of lower-density, background Rb atoms in the chamber. Suppression of superradiant emission is likely due to variations in transition energies across the cold Rydberg atom sample. For initial  $s$  states, these variations are dominated by inhomogeneities in DD exchange interactions within the random ensemble. Such inhomogeneities will necessarily be present in any measurement involving a large number of atoms where the separation between atoms is not well defined. For initial  $p$  states, the suppression is likely due to a combination of DD exchange and electric field inhomogeneities.

# Bibliography

- [1] T. F. Gallagher, *Rydberg Atoms*, 1st ed. (Cambridge University Press, Cambridge, 1994).
- [2] M. D. Lukin, M. Fleischhauer, R. Cote, L. M. Duan, D. Jaksch, J. I. Cirac, and P. Zoller, *Phys. Rev. Lett.* 87, 037901 (2001).
- [3] D. Tong, S. M. Farooqi, J. Stanojevic, S. Krishnan, Y. P. Zhang, R. Cote, E. E. Eyler, and P. L. Gould, *Phys. Rev. Lett.* 93, 063001 (2004).
- [4] F. Robicheaux and J. V. Hernandez, *Phys. Rev. A* 72, 063403 (2005).
- [5] T. Cubel Liebisch, A. Reinhard, P. R. Berman, and G. Raithel, *Phys. Rev. Lett.* 95, 253002 (2005).
- [6] T. Vogt, M. Viteau, J. Zhao, A. Chotia, D. Comparat, and P. Pillet, *Phys. Rev. Lett.* 97, 083003 (2006).
- [7] E. Urban, T. A. Johnson, T. Henage, L. Isenhower, D. D. Yavuz, T. G. Walker, and M. Saffman, *Nat. Phys.* 5, 110 (2009).
- [8] Alpha Gaëtan, Yevhen Miroshnychenko, Tatjana Wilk, Amodsen Chotia, Matthieu Viteau, Daniel Comparat, Pierre Pillet, Antoine Browaeys, and Philippe Grangier, *Nat. Phys.* 5, 115 (2009).
- [9] T. Wilk, A. Gaetan, C. Evellin, J. Wolters, Y. Miroshnychenko, P. Grangier, and A. Browaeys, *Phys. Rev. Lett.* 104, 010502 (2010).
- [10] Hendrik Weimer, Robert Low, Tilman Pfau, and Hans Peter Buchler, *Phys. Rev. Lett.* 101, 250601 (2008).
- [11] M. Saffman and K. Molmer, *Phys. Rev. Lett.* 102, 240502 (2009).

- [12] Robert Low, Hendrik Weimer, Ulrich Krohn, Rolf Heidemann, Vera Bendkowsky, Bjorn Butscher, Hans Peter Buchler, and Tilman Pfau, Phys. Rev. A 80, 033422 (2009).
- [13] T. Pohl and P. R. Berman, Phys. Rev. Lett. 102, 013004 (2009).
- [14] Thomas Amthor, Christian Giese, Christoph S. Hofmann, and Matthias Weidemuller, Phys. Rev. Lett. 104, 013001 (2010).
- [15] T. Pohl, E. Demler, and M. D. Lukin, Phys. Rev. Lett. 104, 043002 (2010).
- [16] S. Wuster, C. Ates, A. Eisfeld, and J. M. Rost, Phys. Rev. Lett. 105, 053004 (2010).
- [17] Jens Honer, Hendrik Weimer, Tilman Pfau, and Hans Peter Buchler, Phys. Rev. Lett. 105, 160404 (2010).
- [18] J. D. Pritchard, D. Maxwell, A. Gauguet, K. J. Weatherill, M. P. A. Jones, and C. S. Adams, Phys. Rev. Lett. 105, 193603 (2010).
- [19] A. Schwarzkopf, R. E. Sapiro, and G. Raithel, Phys. Rev. Lett. 107, 103001 (2011).
- [20] S. Sevincli, N. Henkel, C. Ates, and T. Pohl, Phys. Rev. Lett. 107, 153001 (2011).
- [21] F. Bariani, Y. O. Dudin, T. A. B. Kennedy, and A. Kuzmich, Phys. Rev. Lett. 108, 030501 (2012).
- [22] Matthieu Viteau, Paul Huillery, Mark G. Bason, Nicola Malossi, Donatella Ciampini, Oliver Morsch, Ennio Arimondo, Daniel Comparat, and Pierre Pillet, Phys. Rev. Lett. 109, 053002 (2012).
- [23] D. D. Bhaktavatsala Rao and Klaus Molmer, Phys. Rev. Lett. 111, 033606 (2013).
- [24] H. Schempp, G. Gunter, M. Robert-de-Saint-Vincent, C. S. Hofmann, D. Breyel, A. Komnik, D. W. Schonleber, M. Garttner, J. Evers, S. Whitlock, and M. Weidemuller, Phys. Rev. Lett. 112, 013002 (2014).
- [25] Matthew Ebert, Alexander Gill, Michael Gibbons, Xianli Zhang, Mark Saffman, and Thad G. Walker, Phys. Rev. Lett. 112, 043602 (2014).
- [26] D. Paredes-Barato and C. S. Adams, Phys. Rev. Lett. 112, 040501 (2014).

- [27] H. Gorniaczyk, C. Tresp, J. Schmidt, H. Fedder, and S. Hofferberth, *Phys. Rev. Lett.* 113, 053601 (2014).
- [28] Daniel Tiarks, Simon Baur, Katharina Schneider, Stephan Dürr, and Gerhard Rempe, *Phys. Rev. Lett.* 113, 053602 (2014).
- [29] David Petrosyan and Klaus Molmer, *Phys. Rev. Lett.* 113, 123003 (2014).
- [30] J. Pellegrino, R. Bourgain, S. Jennewein, Y. R. P. Sortais, A. Browaeys, S. D. Jenkins, and J. Ruostekoski, *Phys. Rev. Lett.* 113, 133602 (2014).
- [31] Daniel Barredo, Henning Labuhn, Sylvain Ravets, Thierry Lahaye, Antoine Browaeys, and Charles S. Adams, *Phys. Rev. Lett.* 114, 113002 (2015).
- [32] Y. O. Dudin and A. Kuzmich, *Science* 336, 887 (2012).
- [33] Alexander W. Glaetzle, Marcello Dalmonte, Rejish Nath, Christian Gross, Immanuel Bloch, and Peter Zoller, *Phys. Rev. Lett.* 114, 173002 (2015).
- [34] R. M. W. van Bijnen and T. Pohl, *Phys. Rev. Lett.* 114, 243002 (2015).
- [35] M. Ebert, M. Kwon, T. G. Walker, and M. Saffman, *Phys. Rev. Lett.* 115, 093601 (2015).
- [36] F. Gounand, M. Hugon, P. R. Fournier, and J. Berlande, *J. Phys. B* 12, 547 (1979).
- [37] C. Carr, R. Ritter, C. G. Wade, C. S. Adams, and K. J. Weatherill, *Phys. Rev. Lett.* 111, 113901 (2013).
- [38] R. H. Dicke, *Phys. Rev.* 93, 99 (1954).
- [39] T. Wang, S. F. Yelin, R. Cote, E. E. Eyler, S. M. Farooqi, P. L. Gould, M. Kostrun, D. Tong, and D. Vrinceanu, *Phys. Rev. A* 75, 033802 (2007).
- [40] N. Skribanowitz, I. P. Herman, J. C. MacGillivray, and M. S. Feld, *Phys. Rev. Lett.* 30, 309 (1973).
- [41] M. Gross, C. Fabre, P. Pillet, and S. Haroche, *Phys. Rev. Lett.* 36, 1035 (1976).
- [42] D. Pavolini, A. Crubellier, P. Pillet, L. Cabaret, and S. Liberman, *Phys. Rev. Lett.* 54, 1917 (1985).



- [43] M. G. Moore and P. Meystre, Phys. Rev. Lett. 83, 5202 (1999).
- [44] J. I. Kim, R. B. B. Santos, and P. Nussenzveig, Phys. Rev. Lett. 86, 1474 (2001).
- [45] C. Greiner, B. Boggs, and T. W. Mossberg, Phys. Rev. Lett. 85, 3793 (2000).
- [46] Chiu Fan Lee and Neil F. Johnson, Phys. Rev. Lett. 93, 083001 (2004).
- [47] Vasily V. Temnov and Ulrike Woggon, Phys. Rev. Lett. 95, 243602 (2005).
- [48] J. O. Day, E. Brekke, and T. G. Walker, Phys. Rev. A 77, 052712 (2008).
- [49] Kirill Prozument, Anthony P. Colombo, Yan Zhou, G. B. Park, Vladimir S. Petrovic, Stephen L. Coy, and Robert W. Field, Phys. Rev. Lett. 107, 143001 (2011).
- [50] Anthony P. Colombo, Yan Zhou, Kirill Prozument, Stephen L. Coy, and Robert W. Field, J. Chem. Phys. 138, 014301 (2013).
- [51] Florian Karlewski, Markus Mack, Jens Grimm, Nora Sandor, and Jozsef Fortagh, Phys. Rev. A 91, 043422 (2015).
- [52] N. E. Rehler and J. H. Eberly, Phys. Rev. A 3, 1735 (1971).
- [53] R. Bonifacio and L. A. Lugiato, Phys. Rev. A 11, 1507 (1975).
- [54] Zhi-Gang Feng, Lin-Jie Zhang, Jian-Ming Zhao, Chang-Yong Li, and Suo-Tang Jia, J. Phys. B 42, 145303 (2009).
- [55] K. J. Weatherill, J. D. Pritchard, R. P. Abel, M. G. Bason, A. K. Mohapatra, and C. S. Adams, J. Phys. B 41, 201002 (2008).
- [56] Jianing Han and H. Maeda, Can. J. Phys. 92, 1130 (2014).
- [57] M. R. Kutteruf, Coherence in Rydberg atoms: Measurement and Control, Ph.D. dissertation, University of Virginia (2010).
- [58] B. G. Richards and R. R. Jones (unpublished).
- [59] Wenhui Li, Michael W. Noel, Michael P. Robinson, Paul J. Tanner, Thomas F. Gallagher, Daniel Comparat, Bruno Laburthe Tolra, Nicolas Vanhaecke, Thibault Vogt, Nassim Zahzam, Pierre Pillet, and Duncan A. Tate, Phys. Rev. A 70, 042713 (2004).

- [60] M. P. Robinson, Interactions in a frozen Rydberg gas, Ph.D. dissertation, University of Virginia, 2002.
- [61] F. Gounand, J. Phys. (Paris) 40, 457 (1979).
- [62] M. Gross and S. Haroche, Phys. Rep. 93, 301 (1982).
- [63] M. R. Kutteruf and R. R. Jones, Phys. Rev. A 82, 063409 (2010).
- [64] M. R. Kutteruf and R. R. Jones, Phys. Rev. Lett. 108, 013001 (2012).
- [65] M. L. Zimmerman, M. G. Littman, M. M. Kash, and D. Kleppner, Phys. Rev. A 20, 2251 (1979).

## 5 Rydberg Wavepackets Evolution in A Frozen Gas of DD Coupled Atoms

We have studied the evolution of Rydberg wavepackets in the presence of interatomic dipole- dipole interactions in a frozen Rb gas. Rb atoms in a MOT are first laser-excited to  $ns$  Rydberg eigenstates. A picosecond THz pulse further excites them into coherent superposition states involving the initial-level and neighboring  $np$ -states. A second, identical, time-delayed THz pulse probes the wavepacket dynamics. As the wavepackets evolve they are influenced by dipole-dipole interactions, predominantly pairwise excitation-exchange processes of the form  $|s\rangle|p\rangle \leftrightarrow |p\rangle|s\rangle$ . The coherent electronic evolution of the ensemble dephases due to the variation in dipole-dipole coupling strength between atom pairs in the MOT. The experimental results are in good agreement with numerical calculations that simulate the interactions between nearest neighbors in a frozen gas.

## 5.1 Introduction

As we mentioned in Chapter 3, the large size of Rydberg atoms endows them with extreme properties which, when properly harnessed, can be exploited to study fundamental problems and applications involving the quantum control of matter in single-, few-, and many-body systems. For example, Rydberg atoms are highly-sensitive to applied electric fields and, accordingly, to neighboring atoms, as these can induce substantial energy-shifts and/or quantum-state modification. They also exhibit long electronic time-scales,  $\tau = 2\pi/E$ , which characterize the evolution of superpositions of Rydberg states with small energy separations,  $E$ .

The strong, long-range dipole-dipole interactions that exist between neighboring Rydberg atoms couple their electronic and center-of-mass degrees of freedom [1]. Control over this coupling could enable coherent manipulation of multi-atom correlations and entanglement [2–13] with potential applications to quantum information processing [14–18] or explorations of few- and many-body quantum mechanics. That said, the time- and energy-scales associated with electronic motion within individual atoms can differ substantially from those relevant to dipole-dipole couplings between atoms [1]. This disparity of scales has encouraged the segregation of work in this area, with studies of electron dynamics within atoms performed separately from those investigating interactions between atoms.

For example, in experiments exploring interactions between Rydberg atoms (e.g. resonant energy transfer [19–30], dipole blockade [2, 13, 31–36], quantum-logic gate implementation [14–18]) the interatomic coupling strengths typically range from kHz to tens of MHz with associated time-scales for the development of correlations ranging from tens of nanoseconds to milliseconds. Frequency-domain techniques and cold atomic ensembles are usually employed to enable selective excitation or high-resolution

spectroscopy of the few- or many-body eigenstates and to limit effects associated with atom motion. Since the coupling between atoms depends on their separation, both Rydberg atom density,  $\rho$  and temperature,  $T$ , play an important role as these determine the strength and length-scales of correlations as well as the time-scales over which coherence can be maintained.

Conversely, experiments aimed at coherently manipulating and viewing the evolution of one-electron [37–41] and two-electron [42–52] Rydberg wavepackets typically utilize time- domain methods involving ultra-fast optical and/or electric-field pulses to first excite coherent superposition states and then probe their behavior. For atoms with principal quantum number  $n < 100$  or so, the relevant dynamics in these experiments usually fall in the picosecond or femtosecond regime. Over these time-scales relative atom motion is completely negligible, even in thermal beams. Moreover, interactions between atoms can be ignored since their influence on the electronic evolution develops only after orders of magnitude longer times (tens of nanoseconds to milliseconds).

More generally, however, both ultrafast electron evolution and atom-atom correlations play a role in the quantum dynamics of Rydberg systems. Electron dynamics in isolated atoms set the scale for how rapidly correlations between atoms can be modified, whereas the coupling between atoms determines the minimum-time required for entanglement between pairs or groups of atoms to influence electronic evolution within them. Accordingly, potential applications may require the coherent manipulation of groups, pairs, or individual Rydberg atoms over time- and energy- scales spanning many orders of magnitude. Thus, these systems provide challenging platforms on which to explore few- and many-body quantum control.

As a step towards addressing this problem, we examine the influence of strong, resonant dipole-dipole interactions between atoms on the evolution of Rydberg wavepackets within

those atoms. Specifically, we consider the pulsed, coherent excitation of atoms from a Rydberg eigenstate  $|s\rangle$ , to an adjacent level of opposite parity,  $|p\rangle$ , at time  $t = 0$ . In an extremely diffuse ensemble where the separation between atoms  $R \rightarrow \infty$ , the excitation would result in the creation of identical Rydberg wavepackets in each atom

$$\Psi(t) = \cos\theta|s\rangle + e^{-i(Et+\phi)}\sin\theta|p\rangle \quad (5.1)$$

where  $E$  is the energy separation between the eigenstates,  $\theta$  is an admixture coefficient,  $\phi$  is an arbitrary phase related to the details of the excitation and, unless otherwise noted, atomic units are used throughout. The wavepackets are characterized by identical time-dependent electric dipole-moments which oscillate with a period,  $\tau = 2\pi/E$ .

At higher densities the Rydberg electrons on each atom do not evolve independently. Each electron is affected by the multi-pole fields produced by neighboring Rydberg atoms [1]. The correlations resulting from these interactions can be non-negligible even for separations  $R$  of several microns or more [30]. In the density regime explored here,  $10^8 \times \text{cm}^{-3} < \rho < 3 \times 10^9 \text{ cm}^{-3}$ ,  $R \gg r_0$  where  $r_0 \sim 2n^2$  is the radial extent of the Rydberg wavefunction on each atom. Accordingly, resonant dipole-dipole exchange between nearest-neighbor atoms [23, 24, 27, 53] with a coupling strength on the order of  $n^4/R^3$  ( $\sim 5$  MHz at  $n=30$  and  $\rho = 10^9 \text{ cm}^{-3}$ ), dominates the atom-atom interaction. The coupling alters the eigenstates of atom pairs and, accordingly, modifies the electric-dipole oscillations within them. We measure, as a function of density, the influence of the dipole-dipole exchange interaction on the coherent dipole oscillations in the Rydberg ensemble.

## 5.2 Experimental Procedure

In Chapter 2, we talked about the general experiment setup. More details about the experimental approach of this project is provide below.

In the experiments,  $^{85}\text{Rb}$  atoms at  $\sim 70\ \mu\text{K}$  in a magneto-optical trap (MOT) are laser-excited from the  $5p_{3/2}$  upper cycling-level to the  $32s$  Rydberg state. The atoms are then exposed to a picosecond THz pulse which coherently redistributes a fraction  $\sim 20\%$  of the  $32s$  population to neighboring  $31p$  and  $32p$  levels which lie approximately  $4.79\text{cm}^{-1}$  and  $4.35\text{cm}^{-1}$  below and above the initial state, respectively. Excitation of other levels is negligible. The mixed-parity Rydberg wavepackets are allowed to freely evolve for a variable time  $\Delta t$  before they are subjected to a second, identical THz pulse. The probability amplitude transfer during the second THz pulse interferes with that from the first, resulting in a  $\Delta t$ -dependent modulation in the net population in each Rydberg state. State-selective field ionization (SSFI) is used to measure the final Rydberg eigenstate distribution as a function of  $\Delta t$  and  $\rho$ .

The initial Rydberg excitation is performed using a 10 ns, dye-amplified pulse from a  $\sim 482\ \text{nm}$  cw diode laser. A 10ns pulse is sliced from the cw laser by applying a high-voltage pulse to a Pockells cell that is positioned between crossed polarizers. The two-stage dye-amplifier is pumped at 15 Hz by the third harmonic of a Nd:YAG laser. The 482nm laser pulse is focused into the MOT using a 500 mm spherical lens. The freely propagating picosecond THz pulses are produced via optical rectification of 2 mJ, 150 fs, 790 nm laser pulses in  $\text{LiNbO}_3$ , using a tilted-pulse-front pumping scheme [54, 55]. The 790nm pulses are generated in a 15 Hz Ti:Sapphire regenerative amplifier. A Michelson interferometer, with a variable-length delay-stage in one arm, is used to split each 790 nm pulse into a pump- probe pair with a delay  $0 \leq \Delta t < 16\ \text{ns}$ . The two 790 nm pulses are collinearly incident on the  $\text{LiNbO}_3$  crystal, producing a pair of identical, co-propagating broadband single-cycle THz pulses [56]. After exiting the  $\text{LiNbO}_3$  crystal, the THz beam is collected by a 50 mm diameter, 50 mm focal length off-axis paraboloid. It is then weakly focused by a Teflon lens, through a thin fused silica window, into the MOT. The ramped-field that

performs the SSFI is applied to the atoms approximately 100 ns after the second THz pulse. Four thin, parallel, stainless steel rods are positioned in a rectangular array surrounding the 0.5 mm diameter atom cloud, and enable the application of a spatially-uniform field while providing optical access for the trapping beams, Rydberg excitation laser, and THz pulses. Rb ions produced during the field ramp are pushed toward a micro-channel plate detector and, in principle, population in different Rydberg states can be distinguished by different ionization times in the ramped field. In practice, the signals associated with the  $32s$  and  $31p$  states appear at the same time, thus we do not separately measure the populations in these two states. The delay,  $\Delta t$  between the THz pulses is scanned continuously while integrating the SSFI signals across two time bins, yielding the populations in  $32s+31p$  states and  $32p$  level, respectively. The Rydberg atom density,  $10^8 \text{ cm}^{-3} < \rho < 3 \times 10^9 \text{ cm}^{-3}$ , is varied by changing the current to the getters that supply the Rb atoms to the MOT. At these densities, with  $T = 70 \text{ } \mu\text{K}$ , relative atom motion due to thermal energy or dipole-dipole forces is negligible during the  $\sim 100 \text{ ns}$  duration of the experiments.

### 5.3 Experimental Results

Figure 5.1 shows the measured population in the  $32s+31p$  states as a function of the delay  $\Delta t$  between the two THz pulses. The modulations in the population have a frequency of  $4.35 \text{ cm}^{-1}$ , corresponding to the energy separation between the  $32s$  and the  $32p$  states, and reflect the oscillation of the electric dipole-moment of the wavepacket that is created by the first THz pulse. Oscillations at the same frequency are observed in the  $32p$  population, but are 180 degrees out of phase. The modulations can be interpreted as the result of time-domain Ramsey interference in the  $32s$  and  $32p$  amplitudes created by the first and second THz pulses [57, 58]. Accordingly, the amplitude of the oscillations provides a measure of the macroscopic wavepacket coherence. Although the broadband THz pulses also excites atoms from  $32s$  to  $31p$  we do not observe any significant signal



modulations at  $4.79 \text{ cm}^{-1}$ , the frequency corresponding to the  $32s - 31p$  energy interval. For the weak population transfers studied here, any oscillations in the  $32s$  population would be out of phase with those in  $31p$ , resulting in no net modulation in the combined  $32s+31p$  signal that we detect. Moreover, the small variations in the  $32s$  amplitude associated with the  $31p$  excitation have negligible influence on the population transfer to  $32p$ , so no  $4.79 \text{ cm}^{-1}$  beat is observed in the  $32p$  signal.

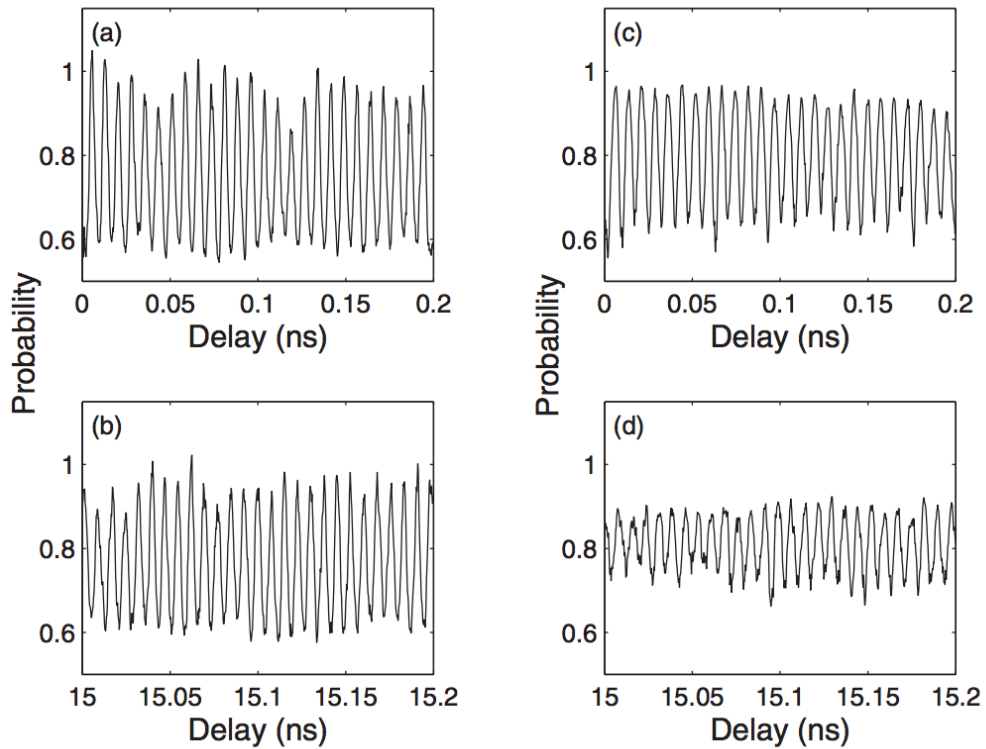


Figure 5.1: Measured population in the combined  $32s+31p$  states as a function of the delay  $\Delta t$  between two THz pulses. The left panels show data collected at low Rydberg density,  $\rho \sim 3 \times 10^8 \text{ cm}^{-3}$ , for (a) short ( $\Delta t \approx 0$ ) and (b) long ( $\Delta t \approx 15 \text{ ns}$ ) delays, respectively. The right panels show data collected at high Rydberg density,  $\rho \sim 2 \times 10^9 \text{ cm}^{-3}$ , for (c) short ( $\Delta t \approx 0$ ) and (d) long ( $\Delta t \approx 15 \text{ ns}$ ) delays, respectively. The decrease in oscillation amplitude at high density and long delays is apparent.

Figure 5.1a and 5.1b show the situation at low density  $\rho \sim 3 \times 10^8 \text{ cm}^{-3}$  for short ( $\Delta t \approx 0$ ) and long ( $\Delta t \approx 15 \text{ ns}$ ) delays, respectively. Analogous plots at higher density  $\rho \sim 2 \times 10^9 \text{ cm}^{-3}$  are shown in Figure 5.1c and 5.1d. At low density, the average oscillation amplitudes are similar at short and long delays. However, at higher densities, there is a notable decrease in oscillation amplitude with increasing delay. This density-dependent decay in the macroscopic wavepacket coherence, i.e. dephasing, is the principal focus of this paper.

To quantify the average oscillation amplitude during a given time interval, we Fourier transform the delay-dependent data, and compute the area under the spectral feature (between  $4.0 \text{ cm}^{-1}$  and  $4.6 \text{ cm}^{-1}$ ) corresponding to the  $32s - 32p$  quantum beat. Figure 5.2 shows the Fourier transforms of the data in Figure 5.1. For each Rydberg density, we compute a decay factor,  $\eta$ , defined as the ratio of the spectral area measured near  $\Delta t = 15 \text{ ns}$  to that measured near  $\Delta t = 0$ .

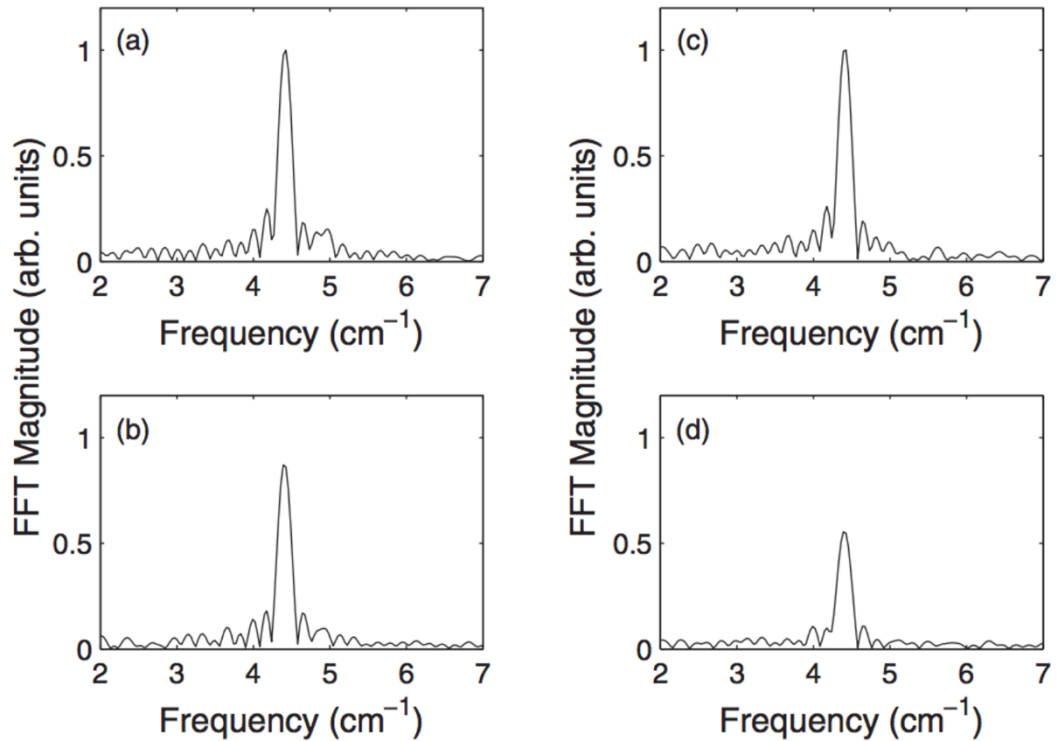


Figure 5.2: Fast Fourier transform (FFT) of the delay-dependent populations shown in Figure 5.1.

The experimentally determined values of  $\eta$  are plotted vs Rydberg density in Figure 5.3 along with the results of a quantum simulation that considers the dipole-dipole interaction between nearest neighbor atoms in a frozen ensemble of randomly distributed Rydberg atoms. The simulation is in good agreement with the measurements. Before discussing the details of the full simulation, we present a simple model that captures the essential physics. Namely, the decrease in  $\eta$  with increasing density is due to the variation in the strength of the dipole-dipole exchange interaction for different pairs of nearest neighbor atoms.

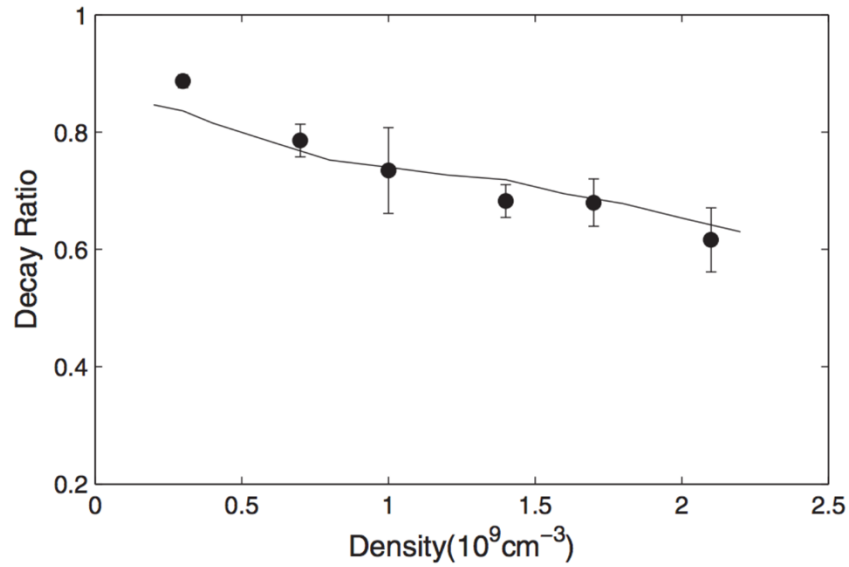


Figure 5.3: Measured (filled circles) and simulated (solid curve) decay ratio,  $\eta$ , as a function of Rydberg density.

## 5.4 Discussion

Consider a two-level Rydberg atom with opposite parity, non-degenerate eigenstates,  $|s\rangle$  and  $|p\rangle$ , that are split by an energy  $E_0$ . Ignoring the azimuthal degrees of freedom, the eigenstates for a pair of atoms with a large separation  $R \rightarrow \infty$  are:  $|ss\rangle$ ,  $|sp\rangle$ ,  $|ps\rangle$ , and  $|pp\rangle$ , with energies as shown on the left in Figure 5.4. For smaller values of  $R$ , the pair eigenstates

are modified due to the interactions between the atoms. Provided that  $R$  remains sufficiently large that the Rydberg wavefunctions of the individual atoms do not overlap, the predominant interaction between the atoms is given by the dipole-dipole coupling [53],

$$V = [\vec{\mu}_A \cdot \vec{\mu}_B - 3(\vec{\mu}_A \cdot \hat{R})(\vec{\mu}_B \cdot \hat{R})]/R^3 \quad (5.2)$$

as we mentioned in Chapter 4. The matrix elements coupling  $|ss\rangle$  or  $|pp\rangle$  to  $|sp\rangle$  and  $|ps\rangle$  are identically zero. In addition, provided  $2E_0$  is much greater than the magnitude of the matrix element connecting  $|ss\rangle$  and  $|pp\rangle$ , the Hamiltonian is approximately diagonalized by considering only the coupling between the degenerate states  $|sp\rangle$ ,  $|ps\rangle$ , i.e. the dipole-dipole exchange interaction. The modified energy levels are shown on the right in Figure 5.4, with eigenstates  $|+\rangle$  and  $|-\rangle$  corresponding to symmetric and antisymmetric combinations of  $|sp\rangle$ ,  $|ps\rangle$ . The exchange splitting between this pair of entangled states is  $2\epsilon = 2\langle ps|V|sp\rangle$  which implicitly depends on the atom separation,  $R$ .

A THz pulse with a central frequency  $E_0$  and a bandwidth  $\gg \epsilon$  can excite the atom pair from  $|ss\rangle$  to  $|+\rangle$ , via a one-photon excitation, or to  $|pp\rangle$  through two-photon absorption. However,  $|-\rangle$  is not populated since the transition matrix elements connecting it to all other levels are identically zero. For a relatively weak THz pulse, the  $|pp\rangle$  excitation probability is negligible, so an electronic coherence is established between  $|ss\rangle$  and  $|+\rangle$ , and the electronic wavefunction has the form,  $\Psi(t) = \cos\theta|ss\rangle + e^{-i(Et+\phi)}\sin\theta|+\rangle$ , where  $\theta$  depends on the excitation probability and  $\phi$  is an excitation phase. This wavepacket has the same form as the single electron wavepacket in Equation (5.1) and, similarly, is characterized by a time-dependent dipole moment which oscillates sinusoidally at a frequency,  $E = E_0 + \epsilon$ . When the atoms are exposed to a second THz pulse, the net population transfer from  $|ss\rangle$  to  $|+\rangle$  is delay- dependent, oscillating at a frequency  $E$ . This modulation can be observed in the total population of individual atoms in states  $|s\rangle$  or  $|p\rangle$ . It can be viewed as the result of time- domain Ramsey interference in the probability

amplitude transferred from  $|ss\rangle$  to  $|+\rangle$  in each of the two THz pulses [57, 58]. Alternatively, but equivalently, it can be attributed to the variations in the wavepacket's instantaneous electric dipole moment during the second THz pulse.

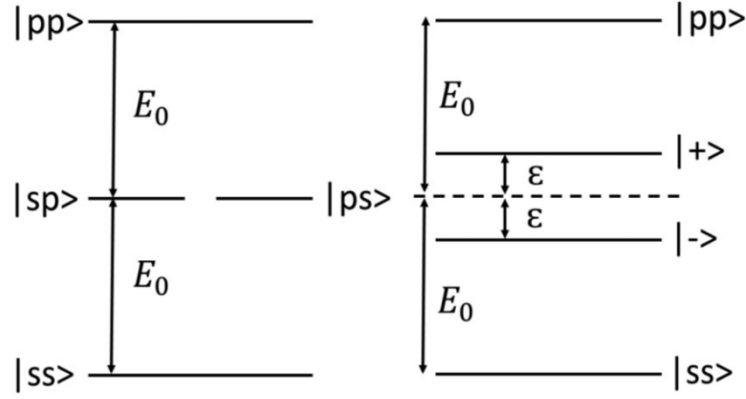


Figure 5.4: Schematic energy level diagram for the eigenstates of a pair of two level atoms. The diagrams on the left and right sides of the figure depict the situation at large and small interatomic spacing,  $R$ , respectively.

In a random ensemble of atoms, the dominant coupling is between each atom and its nearest neighbor. Due to the variation in  $R$  for different atom pairs, there is a broad distribution of dipole-dipole exchange energies  $2\epsilon$  and, accordingly, a range of wavepacket oscillation frequencies  $E$  across the sample. This inhomogeneity results in a dephasing of the detected oscillations in the  $|s\rangle$  and  $|p\rangle$  populations. The dephasing time decreases with increasing Rydberg density, since the range of possible exchange energies grows with the probability of finding atom pairs with smaller  $R$ . It is important to note, however, that the macroscopic dephasing is not an indicator of microscopic decoherence of individual atom pairs.

In the experiments, limitations in the maximum path length difference in the arms of the Michelson interferometer preclude our measurement of the wavepacket evolution from

its initiation through complete dephasing. Instead, we use  $\eta$  as a measure of the dephasing rate. Since smaller values of  $\eta$  reflect more rapid dephasing, the data in Figure 5.3 confirm the qualitative prediction of the model presented in the preceding paragraphs.

To determine if nearest neighbor interactions are sufficient to cause the density-dependent dephasing that is observed, we perform quantum simulations to obtain a quantitative prediction of the dephasing rate. Specifically, we numerically integrate the time-dependent Schroedinger equation to calculate the delay-dependent probability for finding atoms in a range of essential Rydberg states following the exposure of a random ensemble of  $32s$  atoms to two single-cycle THz pulses [56] like those used in the experiments. We include  $33s$ ,  $32p$ ,  $32s$ , and  $31p$  states, with fine-structure, and consider the excitation to, and from, Rydberg-Rydberg pairs with all allowable values of  $M$ , the quantum number corresponding to the projection of total angular momentum along  $\vec{R}$ . Atom pairs with different  $M$  possess different interaction energies, even for the same value of  $R$ , providing an additional source of inhomogeneity in the oscillation frequency of different wavepackets in the ensemble [29, 59]. Radial matrix elements are computed using a Numerov algorithm [60] with the known quantum defects of the Rb  $ns$  and  $np$  states. The simulation results for individual atom pairs are integrated over the nearest neighbor distribution function for  $R$  for a given Rydberg density [61]. Since the quantization axis for each atom pair is chosen to lie along  $\vec{R}$ , the THz polarization angle relative to that axis is varies from one atom pair to the next (refer to 3.3.4). We find that the simulation results are insensitive to whether we explicitly perform the calculation over all polarization angles and average those results, or if we fix the polarization angle at a value for which the interaction potential is equal to angle-averaged value. Since the latter method substantially improves the calculation speed, we use it for the results shown in Figure 5.3.

Inspection of Figure 5.3 shows that the agreement between the data and simulation is good. The fact that there are no adjustable parameters in the calculation, indicates that

nearest neighbor interactions are sufficient to explain the observed dephasing. Beyond the limited pump-probe delay range available to the experiment, the simulations show that the degree and rate of dephasing continue to increase at longer delays and at higher densities, respectively.

## 5.5 Conclusion

We have explored the evolution of Rydberg wavepackets in the presence of strong dipole-dipole interactions in a frozen gas. The time-scales associated with oscillation of the Rydberg electric dipole moment ( $\sim 8$  ps) and the interatomic excitation exchange ( $\sim 200$  ns) differ by over four orders of magnitude yet we are able to probe the system for a sufficiently long time to observe the influence of the atom-atom coupling. The distribution of atom separations results in an inhomogeneity in the strength of the exchange coupling between neighboring atoms, causing a rapid dephasing of the macroscopic coherence. In analogy to recent work with cold polar molecules [62], future experiments may take advantage of optical confinement of atoms at well-defined separations to explore the use of the dipole-dipole coupling as a controllable tool for manipulating multi-electron correlation and dynamics.

# Bibliography

- [1] T. F. Gallagher, Rydberg Atoms, 1st ed. (Cambridge University Press, Cambridge, 1994).
- [2] M. D. Lukin, M. Fleischhauer, R. Cote, L.M. Duan, D. Jaksch, J.I. Cirac, and P. Zoller, Phys. Rev. Lett. 87, 037901 (2001).
- [3] T. Wilk, A. Gaetan, C. Evellin, J. Wolters, Y. Miroshnychenko, P. Grangier, and A. Browaeys, Phys. Rev. Lett. 104, 010502 (2010).
- [4] Hendrik Weimer, Robert Low, Tilman Pfau, and Hans Peter Buchler, Phys. Rev. Lett. 101, 250601 (2008).
- [5] T. Pohl, E. Demler, and M. D. Lukin, Phys. Rev. Lett. 104, 043002 (2010).
- [6] S. Wuster, C. Ates, A. Eisfeld, and J. M. Rost, Phys. Rev. Lett. 105, 053004 (2010).
- [7] Jens Honer, Hendrik Weimer, Tilman Pfau, and Hans Peter Buchler, Phys. Rev. Lett. 105, 160404 (2010).
- [8] A. Schwarzkopf, R. E. Sapiro, and G. Raithel, Phys. Rev. Lett. 107, 103001 (2011).
- [9] Matthieu Viteau, Paul Huillery, Mark G. Bason, Nicola Malossi, Donatella Ciampini, Oliver Morsch, Ennio Arimondo, Daniel Comparat, and Pierre Pillet, Phys. Rev. Lett. 109, 053002 (2012).
- [10] D.D.Bhaktavatsala Rao and K. Molmer, Phys. Rev. Lett. 111, 033606 (2013).
- [11] M. Ebert, A. Gill, M. Gibbons, X. Zhang, M. Saffman, and T.G. Walker, Phys. Rev. Lett. 112, 043602 (2014).
- [12] H. Schempp, G. Gunter, M. Robert-de-Saint-Vincent, C.S. Hofmann, D. Breyel, A. Komnik, D.W. Schonleber, M. Garttner, J. Evers, S. Whitlock, and M. Weidemuller, Phys. Rev. Lett. 112 013002 (2014).



- [13] D. Barredo, S. Ravets, H. Labuhn, L. Beguin, A. Vernier, F. Nogrette, T. Lahaye, and A. Browaeys, Phys. Rev. Lett. 112, 183002 (2014).
- [14] D. Jaksch, J.I. Cirac, P. Zoller, S.L. Rolston, R. Cote, and M.D. Lukin, Phys. Rev. Lett. 85, 2208 (2000).
- [15] M. Muller, I. Lesanovsky, H. Weimer, H. P. Buchler, and P. Zoller, Phys. Rev. Lett. 102, 170502 (2009).
- [16] M. Saffman, T.G. Walker, and K. Molmer, Rev. Mod. Phys. 82, 2313 (2010), and references therein.
- [17] L. Isenhower, E. Urban, X. L. Zhang, A. T. Gill, T. Henage, T. A. Johnson, T. G. Walker, and M. Saffman, Phys. Rev. Lett. 104, 010503 (2010).
- [18] D. Paredes-Barato and C.S. Adams, Phys. Rev. Lett. 112, 040501 (2014).
- [19] K.A. Safinya, J. F. Delpech, F. Gounand, W. Sandner, and T.F. Gallagher, Phys. Rev. Lett. 47, 405 (1981).
- [20] P. Pillet, R. Kachru, N. H. Tran, W. W. Smith, and T. F. Gallagher, Phys. Rev. Lett. 50, 1763 (1983).
- [21] D.S. Thomson, M.J. Renn, and T.F. Gallagher, Phys. Rev. Lett. 65, 3273 (1990).
- [22] M.J. Renn and T.F. Gallagher, Phys. Rev. Lett. 67, 2287 (1991).
- [23] W.R. Anderson, J.R. Veale, and T.F. Gallagher, Phys. Rev. Lett. 80, 249 (1998).
- [24] I. Mourachko, D. Comparat, F. de Tomasi, A. Fioretti, P. Nosbaum, V. M. Akulin, and P. Pillet, Phys. Rev. Lett. 80, 253 (1998).
- [25] T. J. Carroll, K. Claringbould, A. Goodsell, M. J. Lim, and M. W. Noel, Phys. Rev. Lett. 93, 153001 (2004).
- [26] A. Walz-Flannigan, J. R. Guest, J.-H. Choi, and G. Raithel, Phys. Rev. A 69, 063405(2004).
- [27] S. Westermann, T. Amthor, A.L. de Oliveira, J. Deiglmayr, M. Reetz-Lamour, and M. Weidemuller, Eur. Phys. J. D 40, 37 (2006).

- [28] P. Bohlouli-Zanjani, J. A. Petrus, and J. D. D. Martin, Phys. Rev. Lett. 98, 203005 (2007).
- [29] M.R. Kutteruf and R.R. Jones, Phys. Rev. A 82, 063409 (2010).
- [30] M.R. Kutteruf and R.R. Jones, Phys. Rev. Lett. 108, 013001 (2012).
- [31] D. Tong, S.M. Farooqi, J. Stanojevic, S. Krishnan, Y.P. Zhang, R. Cote, E.E. Eyler, and P.L. Gould, Phys. Rev. Lett. 93, 063001 (2004).
- [32] K. Singer, M. Reetz-Lamour, T. Amthor, L.G. Marcassa, and M. Weidemuller, Phys. Rev. Lett. 93, 163001 (2004).
- [33] T. Cubel Liebisch, A. Reinhard, P. R. Berman, and G. Raithel, Phys. Rev. Lett. 95, 253002 (2005).
- [34] T. Vogt, M. Viteau, J. Zhao, A. Chotia, D. Comparat, and P. Pillet, Phys. Rev. Lett. 97, 083003 (2006).
- [35] E. Urban, T.A. Johnson, T. Henage, L. Isenhower, D.D. Yavuz, T.G. Walker and M. Saffman, Nature Physics 5, 110 (2009).
- [36] A. Gatan, Y. Miroshnychenko, T. Wilk, A. Chotia, M. Viteau, D. Comparat, P. Pillet, A. Browaeys and P. Grangier, Nature Physics 5, 115 (2009).
- [37] R.R. Jones and L.D. Noordam, Electronic Wavepackets, Adv. in At. Mol. Opt. Phys. 38, 1 (1997), and references therein.
- [38] F.B. Dunning, J.J. Mestayer, C.O. Reinhold, S. Yoshida, and J. Burgdorfer, J. Phy. B: At. Mol. Opt. Phys. 42, 022001 (2009), and references therein.
- [39] J. Bromage and C.R. Stroud, Jr., Phys. Rev. Lett. 83, 4963 (1999).
- [40] H. Maeda, D.V.L. Norum, and T.F. Gallagher, Science 307, 1757 (2005).
- [41] R.S. Minns, M.R. Kutteruf, H. Zaidi, L. Ko and R.R. Jones, Phys. Rev. Lett. 97, 040504 (2006).
- [42] J.G. Story, D.I. Duncan, and T.F. Gallagher, Phys. Rev. Lett. 71, 3431 (1993).
- [43] D. W. Schumacher, B. J. Lyons, and T. F. Gallagher, Phys. Rev. Lett. 78, 4359 (1997).

- [44] Xin Chen and John A. Yeazell, Phys. Rev. Lett. 81, 5772 (1998).
- [45] R. van Leeuwen, M.L. Bajema, and R.R. Jones, Phys. Rev. Lett. 82, 2852 (1999).
- [46] J.B.M. Warntjes, C. Wesdorp, F. Robicheaux, and L.D. Noordam, Phys. Rev. Lett. 83, 512 (1999).
- [47] J.E. Thoma and R.R. Jones, Phys. Rev. Lett. 83, 516 (1999).
- [48] J.G. Story and H.N. Ereifej, Phys. Rev. Lett. 86, 612 (2001).
- [49] R. van Leeuwen, K. Vijayalakshmi, and R.R. Jones, Phys. Rev. A 63, 033403 (2001).
- [50] S.N. Pisharody and R.R. Jones, Phys. Rev. Lett. 91, 203002 (2003).
- [51] S.N. Pisharody and R.R. Jones, Science 303, 813 (2004).
- [52] X. Zhang, R.R. Jones, and F. Robicheaux, Phys. Rev. Lett. 110, 023002 (2013).
- [53] F. Robicheaux, J. V. Hernandez, T. Topcu, and L. D. Noordam, Phys. Rev. A 70, 042703 (2004).
- [54] J. Hebling, Ka-Lo Yeh, M.C. Hoffmann, B. Bartal, and K. A. Nelson, JOSA B, 25, B6 (2008).
- [55] H. Hirori, A. Doi, F. Blanchard, and K. Tanaka, Appl. Phys. Lett. 98, 091106 (2011).
- [56] S. Li and R.R. Jones, Phys. Rev. Lett. 112, 143006 (2014).
- [57] L.D. Noordam, D.I. Duncan, and T.F. Gallagher, Phys. Rev. A 45, 4734 (1992).
- [58] N.E. Tielking and R.R. Jones, Phys. Rev. A 52, 1371 (1995).
- [59] H. Park and T.F. Gallagher, Phys. Rev. A 86, 052510 (2012).
- [60] M.L. Zimmerman, M.G. Littman, M.M. Kash, and D. Kleppner, Phys. Rev. A 20, 2251 (1979).
- [61] P. Hertz, Math. Ann. 67 387 (1909).
- [62] B. Yan, S.A. Moses, B. Gadway, J.P. Covey, K.R.A. Hazzard, A.M. Rey, D.S. Jin, and J. Ye, Nature 501, 521 (2013).